



This is a repository copy of *Structural evolution of synthetic alkali-activated CaO-MgO-Na<sub>2</sub>O-Al<sub>2</sub>O<sub>3</sub>-SiO<sub>2</sub> materials is influenced by Mg content.*

White Rose Research Online URL for this paper:  
<http://eprints.whiterose.ac.uk/117704/>

Version: Accepted Version

---

**Article:**

Walkley, B. [orcid.org/0000-0003-1069-1362](https://orcid.org/0000-0003-1069-1362), San Nicolas, R., Sani, M.A. et al. (3 more authors) (2017) Structural evolution of synthetic alkali-activated CaO-MgO-Na<sub>2</sub>O-Al<sub>2</sub>O<sub>3</sub>-SiO<sub>2</sub> materials is influenced by Mg content. *Cement and Concrete Research*, 99. pp. 155-171. ISSN 0008-8846

<https://doi.org/10.1016/j.cemconres.2017.05.006>

---

Article available under the terms of the CC-BY-NC-ND licence  
(<https://creativecommons.org/licenses/by-nc-nd/4.0/>)

**Reuse**

Items deposited in White Rose Research Online are protected by copyright, with all rights reserved unless indicated otherwise. They may be downloaded and/or printed for private study, or other acts as permitted by national copyright laws. The publisher or other rights holders may allow further reproduction and re-use of the full text version. This is indicated by the licence information on the White Rose Research Online record for the item.

**Takedown**

If you consider content in White Rose Research Online to be in breach of UK law, please notify us by emailing [eprints@whiterose.ac.uk](mailto:eprints@whiterose.ac.uk) including the URL of the record and the reason for the withdrawal request.



[eprints@whiterose.ac.uk](mailto:eprints@whiterose.ac.uk)  
<https://eprints.whiterose.ac.uk/>



25 simply bulk composition, so that the desired binder structure for a particular application can be  
26 achieved.

27

## 28 1. Introduction

29 Alkali-activated materials (AAM) and geopolymers have received significant academic and  
30 commercial interest in recent years due to desirable physical properties, wide-ranging applications  
31 and low embodied CO<sub>2</sub> [1]. The main binding phase in alkali-activated slag is a calcium (alkali)  
32 aluminosilicate hydrate gel (C-(N)-A-S-H), and study of the nanostructure and phase assemblage of  
33 this gel within alkali-activated slags has received significant attention [2-7]. Nanostructural  
34 development of C-(N)-(A)-S-H is strongly dependent on the chemistry of the precursor material [8-  
35 10], and most studies have focused on investigating reaction products within the quaternary CaO-  
36 Na<sub>2</sub>O-Al<sub>2</sub>O<sub>3</sub>-SiO<sub>2</sub> system.

37 However, a significant quantity of magnesium can also be present in blast furnace slags, and this  
38 plays a significant role in formation and evolution of layered double hydroxides (LDH) as the reaction  
39 proceeds. Formation of LDH, in particular hydrotalcite-group phases, modifies the phase assemblage  
40 and consequently performance of alkali-activated slags [10]. The content of magnesium varies  
41 significantly between commercial slags, with the majority of European, Asian and North American  
42 slags containing around 7-14 wt. % MgO [8-11]. Despite the vast number of studies investigating the  
43 chemistry of alkali-activated slags, few have directly investigated the role of magnesium in  
44 nanostructural development in these materials [5, 8, 10, 12, 13]. This is compounded by the lack of  
45 consistency in experimental parameters due to variations in precursor chemistry and the presence  
46 of additional minor constituents in the slags used.

47 Previous attempts to constrain these parameters have involved synthesis of AAM precursor powders  
48 and binder phases in the laboratory under controlled conditions [14-18]. Most commonly a sol-gel

49 procedure is used to form aluminosilicate or calcium-aluminosilicate gels designed to simulate AAM  
50 binder phases and investigate the effect of alkali cations, alkaline earth cations or aluminium on  
51 calcium silicate hydrate (C-S-H) or alkali-aluminosilicate hydrate (N-A-S-H) type gels. This is achieved  
52 by addition of these ions after formation of the gel (either by direct addition of an ion source or by  
53 mixing two different gels together), which restricts the ability to control stoichiometry and  
54 homogeneity in these systems, as well as possibly modifying the structural roles of the cations. The  
55 use of high liquid/solid ratios and the presence of nitrates in many of these systems can also  
56 significantly affect the mechanisms of dissolution, reaction and phase formation [19, 20]. In most  
57 AAM systems, reactive species are initially present and participate simultaneously in the reaction.  
58 This leads to possible differences in the structure of the binder gel networks formed when  
59 comparing the aforementioned synthetic gels to 'real-world' AAM systems, if the degree of  
60 approach to thermodynamic equilibrium is restricted by transport or kinetic limitations.

61 Replication of the physicochemical interactions occurring during alkali-activation of aluminosilicate-  
62 based precursors and subsequent formation of cementitious materials has recently been achieved  
63 by alkali-activation of high-purity synthetic precursor powders [21-23]. The study presented here  
64 extends this work by investigating the next level of complexity in synthetic AAM systems. The effects  
65 of variations in precursor Mg, Ca, Si and Al content on the phase assemblage and nanostructure of C-  
66 (N)-(A)-S-H type gels and additional reaction products are examined using high-purity synthetic  
67 AAMs. These AAMs are synthesised under the same physicochemical conditions which prevail during  
68 alkali-activation of calcium aluminosilicate precursors such as ground granulated blast furnace slag  
69 (GGBFS), i.e., reaction of an aluminosilicate precursor with an alkaline solution. Nanostructural and  
70 spectroscopic characterisation techniques including solid state  $^{29}\text{Si}$ ,  $^{27}\text{Al}$ ,  $^{23}\text{Na}$  magic angle spinning  
71 (MAS) nuclear magnetic resonance (NMR) spectroscopy are used to gain novel insight into the  
72 nanostructural changes occurring during reaction and evolution of these materials, and specifically  
73 to examine the importance of Mg in controlling the nanostructural development of AAM binder  
74 phases.

## 75 2. Experimental Procedures

### 76 2.1 Alkali-activated material synthesis

77 Precursors were synthesised via an organic steric entrapment solution-polymerisation route [24],  
78 with compositions chosen to exhibit chemistry in regions of the CaO-MgO-Na<sub>2</sub>O-Al<sub>2</sub>O<sub>3</sub>-SiO<sub>2</sub> system  
79 which are important for studying C-(N)-(A)-S-H type gels and LDH (Table 2; detailed compositional  
80 analysis of as-synthesised powders in Supporting Information, Table S1). In particular, the Al/Si ratios  
81 represent values expected for non-crosslinked C-(N)-A-S-H (approximately Al/Si ≤ 0.10) and  
82 crosslinked C-(N)-A-S-H gels (approximately 0.10 ≤ Al/Si ≤ 0.20) [2, 25, 26]. The Al/Si, Ca/(Al+Si) and  
83 Mg/(Al+Si) ratios in the samples investigated here also span the range of bulk compositional ratios  
84 observed in Na<sub>2</sub>O·xSiO<sub>2</sub>·yH<sub>2</sub>O activated slags (Al/Si ≤ 0.25, 0.67 ≤ Ca/(Al+Si) ≤ 1.2 and Mg/(Al+Si) ≤  
85 0.40) [2, 4, 8, 10, 27-29], laboratory synthesised calcium aluminosilicates hydrate (C-A-S-H) type gels  
86 (Al/Si ≤ 0.2 and 0.5 ≤ Ca/(Al+Si) ≤ 1) [25, 30-35], and synthetic AAMs (Al/Si ≤ 0.15, 0.67 ≤ Ca/(Al+Si) ≤  
87 1.0) [23, 36].

88 A 5 wt. % polyethylene glycol (PEG) solution was produced by adding PEG (Sigma Aldrich, MW 20  
89 kDa) to distilled water. The polymer was added to distilled water in small increments over heat, and  
90 the resultant solution was stirred at 60 °C for 1 hour. Aluminium nitrate nonahydrate, Al(NO<sub>3</sub>)<sub>3</sub>·9H<sub>2</sub>O  
91 (Sigma Aldrich, 98.5 wt. %), calcium nitrate tetrahydrate, Ca(NO<sub>3</sub>)<sub>2</sub>·4H<sub>2</sub>O (BDH Prolabo, VRW  
92 International, 99.0 wt. %) and magnesium nitrate hexahydrate, Mg(NO<sub>3</sub>)<sub>2</sub>·6H<sub>2</sub>O (Sigma Aldrich, 99.0  
93 wt. %) were each added to distilled water to produce 40 wt.% solutions by mass of anhydrous salt,  
94 and these solutions were subsequently added to the 5 wt. % PEG solution and stirred at 60 °C for  
95 one hour before addition of colloidal silica (Sigma Aldrich Ludox HS-40 colloidal silica (SiO<sub>2</sub>), 40 wt.%  
96 in water). The stoichiometry was designed to achieve the elemental ratios outlined in Table 1, as  
97 well as ensuring that the number of metal cations (M<sup>x+</sup>) in solution was significantly more than the  
98 number that PEG polymer carrier could chemically bind through its OH groups (M<sup>x+</sup>/OH = 2). Water  
99 was evaporated from the resulting solution by stirring over heat at 80 °C to form a viscous aerated

100 gel which was then placed in a drying oven at 100 °C overnight to remove any remaining water. The  
 101 dry aerated gel was then calcined at 3 °C/min to 900 °C in a laboratory muffle furnace, with a 1 hour  
 102 hold time at 900 °C and then cooling in air, producing a fine white powder which was subsequently  
 103 ground by hand before alkali-activation.

104 **Table 1: Molar ratios, polymer carrier and metal valence ( $M^{x+}$ ) to hydroxyl functionality (OH) ratio for each sample**

Sample	Empirical formula	Ca/(Al+Si)	Al/Si	Polymer	$M^{x+}/OH$
A	$2SiO_2 \cdot Al_2O_3$	0.000	1.000	PVA	4
B	$4SiO_2 \cdot Al_2O_3$	0.000	0.500	PVA	4
C	$0.800CaO \cdot SiO_2 \cdot 0.078Al_2O_3$	0.692	0.156	PEG	2
D	$1.214CaO \cdot SiO_2 \cdot 0.078Al_2O_3$	1.050	0.156	PEG	2
E	$0.709CaO \cdot SiO_2 \cdot 0.026Al_2O_3$	0.675	0.051	PEG	2
F	$1.104CaO \cdot SiO_2 \cdot 0.026Al_2O_3$	1.050	0.051	PEG	2

105

106 The activating solution was prepared by dissolving sodium hydroxide powder (AnalaR, 99 wt. %) in a  
 107 sodium silicate solution (Grade N, 37.5 wt. % solids, PQ Australia) and distilled water. Stoichiometry  
 108 was designed to obtain an activating solution modulus of  $SiO_2/Na_2O = 1$ , and cation and water/solids  
 109 (w/s) ratios as outlined in Table 2. The activating solution was mixed with the precursor powder to  
 110 form a homogeneous paste, which was cast in sealed containers and cured at ambient temperature  
 111 ( $\sim 23^\circ C$ ) for 3, 28 and 180 days. The w/s ratios were chosen to enable mixing to form a homogeneous  
 112 paste and formation of a solid binder after curing for 3 days. Changes in C-S-H gel microstructure  
 113 have been observed when using differing w/s ratios during PC hydration [37], however previous  
 114 work has shown that the difference in w/s ratios did not affect the degree of dissolution of these  
 115 precursor powders during the alkali-activation reaction [21-23]. Bound water forms an integral part  
 116 of the C-S-H [38] and C-(N)-A-S-H gel microstructure [39], whereas in N-A-S-H gels water exists  
 117 absorbed inside pores or as hydroxyl groups sorbed to the gel surface [39-41]. Consequently  
 118 variation in w/s ratios of the C-(N)-A-S-H/N-A-S-H gel blends examined in this study are unlikely to  
 119 alter gel microstructure to the same extent as occurs in hydrated PC, however these changes cannot  
 120 be completely ruled out.

**Table 2:** Composition and physical properties of powdered precursors and reaction mixture molar ratios

Sample	Precursor			Reaction mixture				
	Empirical formula	Surface area (m <sup>2</sup> /g)	d <sub>50</sub> (µm)	Ca/(Al+Si)	Al/Si	Na/Al	Mg/(Al+Si)	w/s
A	0.0525MgO·0.7025CaO·SiO <sub>2</sub> ·0.025Al <sub>2</sub> O <sub>3</sub>	1.58	39.9	0.67	0.05	0.50	0.05	0.50
B	0.1575MgO·0.7025CaO·SiO <sub>2</sub> ·0.025Al <sub>2</sub> O <sub>3</sub>	3.82	48.8	0.67	0.05	0.50	0.15	0.63
C	0.2625MgO·0.7025CaO·SiO <sub>2</sub> ·0.025Al <sub>2</sub> O <sub>3</sub>	6.41	28.1	0.67	0.05	0.50	0.25	0.63
D	0.0578MgO·0.7704CaO·SiO <sub>2</sub> ·0.075Al <sub>2</sub> O <sub>3</sub>	2.98	38.6	0.67	0.15	0.50	0.05	0.75
E	0.1725MgO·0.7704CaO·SiO <sub>2</sub> ·0.075Al <sub>2</sub> O <sub>3</sub>	3.81	29.2	0.67	0.15	0.50	0.15	0.75
F	0.2873MgO·0.7704CaO·SiO <sub>2</sub> ·0.075Al <sub>2</sub> O <sub>3</sub>	3.60	25.9	0.67	0.15	0.50	0.25	0.75
G	0.0525MgO·1.050CaO·SiO <sub>2</sub> ·0.025Al <sub>2</sub> O <sub>3</sub>	1.80	43.0	1.00	0.05	0.50	0.05	0.75
H	0.1575MgO·1.050CaO·SiO <sub>2</sub> ·0.025Al <sub>2</sub> O <sub>3</sub>	4.81	27.6	1.00	0.05	0.50	0.15	0.83
I	0.2625MgO·1.050CaO·SiO <sub>2</sub> ·0.025Al <sub>2</sub> O <sub>3</sub>	6.55	31.3	1.00	0.05	0.50	0.25	0.75
J	0.0578MgO·1.150CaO·SiO <sub>2</sub> ·0.075Al <sub>2</sub> O <sub>3</sub>	3.42	27.1	1.00	0.15	0.50	0.05	0.83
K	0.1725MgO·1.150CaO·SiO <sub>2</sub> ·0.075Al <sub>2</sub> O <sub>3</sub>	5.50	59.1	1.00	0.15	0.50	0.15	1.00
L	0.2873MgO·1.150CaO·SiO <sub>2</sub> ·0.075Al <sub>2</sub> O <sub>3</sub>	3.97	60.3	1.00	0.15	0.50	0.25	1.13

122

123 *2.2 Characterisation*

124 For all characterisation techniques except environmental scanning electron microscopy/energy  
125 dispersive X-ray spectroscopy (ESEM/EDX), the hardened pastes were ground by hand using a  
126 mortar and pestle and immersed in acetone for 15 minutes to remove free and loosely bound water  
127 and halt the alkali-activation reaction, then filtered and stored sealed in a desiccator. This method  
128 does not induce significant changes in the AAM gel structure [42].

129 Chemical composition data of the precursors were obtained by energy dispersive X-ray Fluorescence  
130 (XRF) spectrometry using a Spectro 'Xepos' instrument. Sample preparation involved fusion with a  
131 12:22 lithium tetraborate:metaborate flux (XRF Scientific, 35.3 wt. % lithium tetraborate, 64.7 wt. %  
132 lithium metaborate) in platinum crucibles at 1050°C for 15 minutes to produce a glass bead.

133 The Brunauer-Emmett-Teller (BET) surface area [43] of each powder was determined by nitrogen  
134 sorption on a Micromeritics (Norcross, GA) ASAP2010 instrument. The particle size distribution of  
135 the powders was determined using a Malvern Mastersizer 3000 laser diffraction particle size  
136 analyser employing ultrasonic dispersion and assuming a refractive index of 1.62 [44]. Samples were  
137 ground by hand using a mortar and pestle.

138 Differential thermogravimetric analysis was performed on powdered samples of approximately 30  
139 mg in an alumina crucible using a Perkin Elmer Diamond instrument, using a heating rate of 3°C/min  
140 from 30°C to 1000°C, in air, after holding at 30°C for 20 minutes prior to the commencement of  
141 heating. X-ray diffraction (XRD) experiments were performed using a Bruker D8 Advance instrument  
142 with Cu K $\alpha$  radiation, a nickel filter, a step size of 0.020°, a dwell time of 1 second and a 2 $\theta$  range of 3  
143 - 70°. Sample holder background was measured under the same conditions and parameters and  
144 subtracted from each XRD curve prior to normalisation by dwell time.

145 Environmental scanning electron microscopy (ESEM) was conducted using an FEI Quanta instrument  
146 with a 15 kV accelerating voltage and a working distance of 10 mm. To avoid the need for conductive  
147 coating, the samples were cut and immediately evaluated in a low vacuum mode (0.5 mbar water  
148 pressure) using a backscatter detector. A Link-Isis (Oxford Instruments) X-ray energy dispersive (EDX)  
149 detector was used to determine chemical compositions. A random selection of points evenly  
150 distributed across a representative 500  $\mu\text{m}$   $\times$  500  $\mu\text{m}$  section of the sample were used for analysis.

151 Attenuated total reflection Fourier transform infrared (ATR-FTIR) spectra were measured using a  
152 Varian FTS 7000 spectrometer with a Specac MKII Golden Gate single reflectance ATR attachment  
153 with KRS-5 optics and diamond ATR crystal, scanning 32 times at a resolution of 4  $\text{cm}^{-1}$ .

154 Solid state single pulse  $^{29}\text{Si}$ ,  $^{27}\text{Al}$ , and  $^{23}\text{Na}$  MAS NMR spectra were collected on an Agilent VNMRs-  
155 600 spectrometer at 14.1 T ( $B_0$ ) using a 4.0 mm triple resonance bioMAS probe. Parameters for each  
156 experiment are outlined in Table 3. All data were processed using NMRPipe [45].

157

158 **Table 3:** Parameters for each single pulse MAS NMR experiment. Tetramethylsilane (TMS), powdered aluminium chloride  
 159 hexahydrate ( $\text{AlCl}_3 \cdot 6\text{H}_2\text{O}$ ) and powdered sodium chloride (NaCl) were used as reference compounds, as indicated.

Nucleus	Field strength (T)	Transmitter frequency (MHz)	$\pi/2$ pulse width ( $\mu\text{s}$ )	Relaxation delay (s)	Scans	Spinning speed (kHz)	Reference ( $\delta_{\text{iso}}$ / ppm)
$^{29}\text{Si}$	14.1	119.14	7.0	120	1024	10.0	TMS (0.0 ppm)
$^{27}\text{Al}$	14.1	156.26	4.0	2	1024	12.0	$\text{AlCl}_3 \cdot 6\text{H}_2\text{O}_{(s)}$ (0.0 ppm)
$^{23}\text{Na}$	14.1	158.63	5.0	3	512	12.0	$\text{NaCl}_{(s)}$ (7.2 ppm) [46]

160

### 161 3. Results and discussion

#### 162 3.1 X-ray Diffraction

163 X-ray diffractograms of the precursors and AAMs cured for 3, 28 and 180 days are presented in  
 164 Figure 1. Alkali-activation of all samples produces a broad feature from approximately  $15 - 45^\circ 2\theta$ ,  
 165 centred at approximately  $29^\circ 2\theta$ , indicating formation of a disordered reaction product consistent  
 166 with that formed during alkali-activation of GGBFS [10, 29]. A broad peak in the centre of this  
 167 feature is assigned to a poorly crystalline C-(A)-S-H phase displaying some structural similarity with  
 168 aluminium-containing tobermorite (PDF # 19-0052) [36], formed due to the dissolution and reaction  
 169 of the amorphous phase from the precursor powder as well as the dicalcium silicate ( $\text{Ca}_2\text{SiO}_4$ ,  
 170 Powder Diffraction File (PDF) cards:  $\beta$  polymorph # 33-0302 and  $\alpha'_L$  polymorph PDF # 36-0642),  
 171 tricalcium aluminate ( $\text{Ca}_3\text{Al}_2\text{O}_6$ , cubic polymorph, PDF # 38-1429) and free lime (CaO, PDF # 48-1467)  
 172 present in the precursor powders. As the samples aged, the reflection assigned to the C-(A)-S-H type  
 173 gel sharpens and intensifies, indicating increased formation and ordering of this phase as the  
 174 reaction progresses.



178 Small traces of gehlenite ( $\text{Ca}_2\text{Al}(\text{AlSiO}_7)$ ) (PDF # 35-0755) and åkermanite ( $\text{Ca}_2\text{MgSi}_2\text{O}_7$ ) (PDF # 98-  
179 000-0030) are also identified in all precursor powders, as is wollastonite (PDF # 42-0547). The  
180 intensity of the reflections due to each of these crystalline phases do not change upon alkali-  
181 activation or further curing.

182 Monocarbonate AFm (Mc,  $\text{Ca}_4\text{Al}_2(\text{OH})_{12}\cdot\text{CO}_3\cdot x\text{H}_2\text{O}$ ) is observed in most alkali-activated samples with  
183 the exception of samples A and G, while hydroxy-AFm ( $\text{C}_4\text{AH}_{13}$ ) (PDF # 02-0077) is observed to  
184 varying degrees in all alkali-activated samples. Calcite (PDF # 47-1743) also contributes a reflection  
185 at approximately  $29.3^\circ 2\theta$  in the X-ray diffractograms of the AAMs.

186 A reflection assigned to hydrotalcite-group phases ( $\text{Mg}_x\text{Al}_y\text{CO}_3(\text{OH})_{16}\cdot 4(\text{H}_2\text{O})$ ; PDF # 41-1428) is  
187 observed to varying degrees in all these alkali-activated samples; hydrotalcite-group phases  
188 ( $\text{Mg}/\text{Al}\approx 2$ ) have been widely observed in binders produced from slags activated with sodium silicate,  
189 sodium hydroxide and sodium carbonate [13, 19, 47]. These phases generally have  $\text{Mg}/\text{Al}\approx 2$ ,  
190 compared with a ratio of 3 for true hydrotalcite [10, 13, 19, 47].

191 Comparison of the intensity of the reflections attributed to hydrotalcite reveals some key trends.  
192 When the bulk calcium and aluminium content in the precursor powder are held constant, a lower  
193 content of magnesium in the precursor powder promotes formation of more hydrotalcite-group  
194 phases during alkali-activation, while a higher content of magnesium in the precursor powder does  
195 not lead to the formation of crystalline hydrotalcite-group phases. This contrasts with observations  
196 in alkali-activated GGBFS, where (as would be expected from simple chemical arguments) increased  
197 magnesium content (in the presence of sufficient Al) results in the formation of increased amounts  
198 of hydrotalcite-group phases [10]. However, in the samples here, an increase in bulk magnesium  
199 content has resulted in increased formation of melilite-group phases (marked as gehlenite and  
200 åkermanite in Figure 1) during synthesis and calcination of the precursor powder. Consequently, it is  
201 likely the amount of aluminium and magnesium available to participate in the reactions of these  
202 high-Mg powders during alkali-activation at early age is significantly reduced, causing a reduction in  
203 the amount of crystalline hydrotalcite-group phases observed, although XRD does not enable

204 comment on the potential formation of non-crystalline phases of comparable chemistry. This trend  
205 is particularly evident in samples containing higher contents of bulk Al (Al/Si = 0.15, Figure 1 D - F  
206 and J - L).

207 Examining the effect of varying bulk Mg content in samples containing high contents of Ca (i.e.,  
208  $\text{Ca}/(\text{Al}+\text{Si}) = 1.00$  in samples G - L (Figure 1 G - L)) reveals complex interplay between Mg and Ca  
209 constituents. The formation of gehlenite and åkermanite during precursor synthesis is much less in  
210 these high-Ca containing samples. Consequently, these samples will contain more Mg within the  
211 glassy phase of the precursors than samples containing less bulk Ca, and hence this Mg within the  
212 glassy phase can be considered 'freely available' as dissolution of this phase will occur much faster  
213 than Mg-containing crystalline phases in the precursor (which do not appear to participate in the  
214 alkali-activation reaction on the timescales examined here). Despite this, a higher content of  
215 magnesium in the precursor powder has once again resulted in less formation of hydrotalcite-group  
216 phases and C-(A)-S-H, and also greater formation of portlandite due to hydration of  $\text{Ca}_2\text{SiO}_4$ . This  
217 suggests that magnesium also plays an important role in determining the formation of magnesium-  
218 free additional reaction products, such as AFm-type phases, through controlling the availability of  
219 other elements for reaction.

220

### 221 *3.2 Differential Thermogravimetric Analysis*

222 The DTG curves of all precursor samples are relatively flat and featureless with the exception of a  
223 mass loss peak at approximately 680 °C in some precursors, attributed to  $\text{CaCO}_3$  formed due to  
224 reaction of free lime with  $\text{CO}_2$  released during calcination of the precursor during precursor synthesis  
225 [24]. Minor disordered carbonate-containing or hydrous phases, potentially residual polymer from  
226 the synthesis process, lead to small mass loss features in the DTG data at approximately 280 °C for  
227 precursor D, and at approximately 420 °C for precursors J, K and L [24].

228 DTG curves of all AAM at all curing ages assessed display a broad mass loss peak between 50 °C and  
229 200 °C consisting of individual mass loss peaks attributed to water adsorbed or bound to the binder

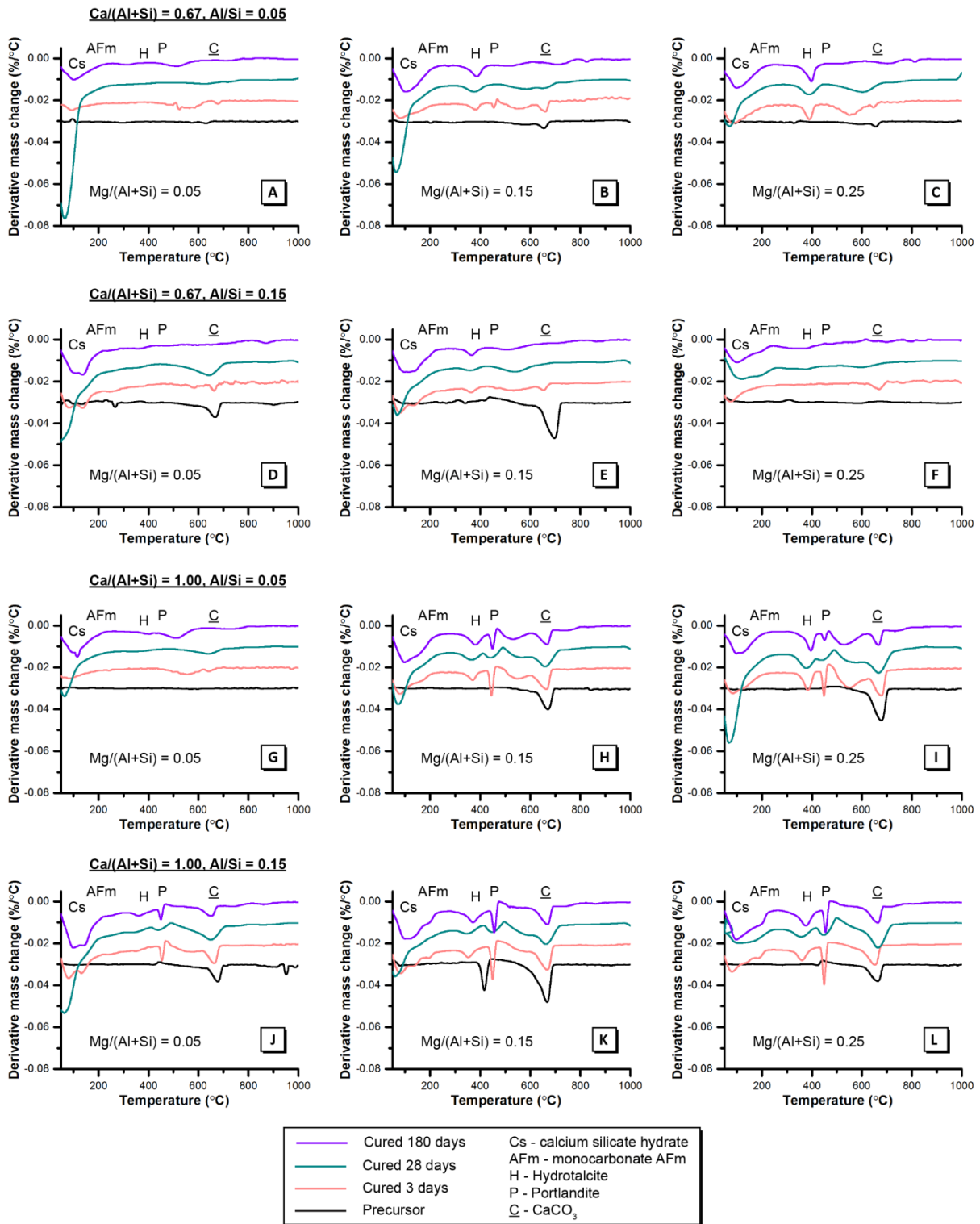
230 phases to varying degrees. Mass loss peaks at approximately 75 °C in the DTG curves of the alkali-  
231 activated material are attributed to the removal of adsorbed atmospheric water from the binder.

232 Mass loss peaks centred at 130 °C in the DTG data for samples produced with powders containing  
233 high bulk Al (i.e., D, E, F, J, K and L, in Figure 2) are attributed to dehydration of free and loosely  
234 bound water originally supplied by the activating solution and present in the pore network of the  
235 binder [48-50], dehydration of the AFm-type phases identified in these samples by XRD [51], and  
236 initial dehydration of the C-(A)-S-H type gel [50]. A progressive mass loss above 380 °C indicates  
237 further dehydration of C-(A)-S-H gel [52]. The dehydration of  $C_4AH_{13}$  and related carboaluminate  
238 phases occurs between 220 °C and 280 °C [53], as identified in Figure 2 for samples K and L at all  
239 curing ages.

240 A sharp mass loss peak due to dehydroxylation of portlandite is observed at 450 °C [50] in the DTG  
241 curves for AAMs H - L at all curing ages (Figure 2), and is also evident in sample B cured for 3 days.  
242 The intensity of this peak decreases from 3 to 180 days; the 28-day samples appear to contain less  
243 portlandite than those cured for 180 days but this is ascribed to differences in carbonation prior to  
244 or during analysis, as some of the portlandite was likely converted to calcite by reaction with  $CO_2$   
245 from the atmosphere. A decrease in portlandite content as samples age is expected due to a process  
246 similar to the pozzolanic reaction, involving the Ca-rich hydration products of the rapidly-reacting  
247 crystalline phases, and the slower-reacting siliceous components. These trends are consistent with  
248 the intensity of the reflections assigned to portlandite in the XRD data for these samples. Portlandite  
249 is not observed in the other samples.

250 Mass loss peaks at approximately 200 °C and 380 °C are observed in the DTG curves for samples  
251 produced with powders containing high bulk Al content (D, E, F, and J, K L) and are assigned to  
252 hydrotalcite-group phases [8, 54, 55], while DTG peaks at approximately 820 °C in the curves  
253 samples A - F cured for 180 days are attributed to decomposition of C-(A)-S-H type gel to  
254 wollastonite [56, 57]. The DTG curves of the alkali-activated material for each sample cured for 28  
255 and 180 days are similar to the 3-day data, with mass loss once again predominantly occurring below

256 200°C. Slight shifts in the temperatures of the low-temperature peaks are evident for each sample,  
 257 and suggest that structural rearrangement continues to occur during curing up to 180 days.



258

259 **Figure 2:** Differential thermogravimetric curves for the precursor powders A-L, and the respective alkali-activated materials  
 260 cured for 3, 28 and 180 days.

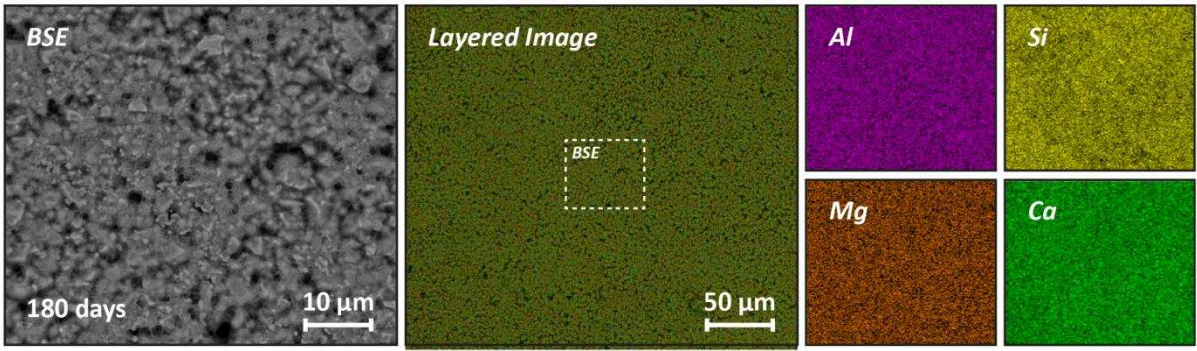
261

262 *3.3 Environmental scanning electron microscopy/energy dispersive X-ray spectroscopy*

263 Back-scattered electron (BSE) images of selected representative samples (A, D and L) cured for 180  
264 days are shown in Figure 3 - Figure 5; corresponding images for the other samples are presented in  
265 Appendix B, Supporting Information. Each micrograph shows a porous, particulate structured AAM.  
266 The C-(A)-S-H type gel exhibits a globular, fibrous morphology (Figure 6) similar to that observed in  
267 alkali-activated slag cements produced using slags containing approximately 8 wt. % MgO [6, 8, 9]

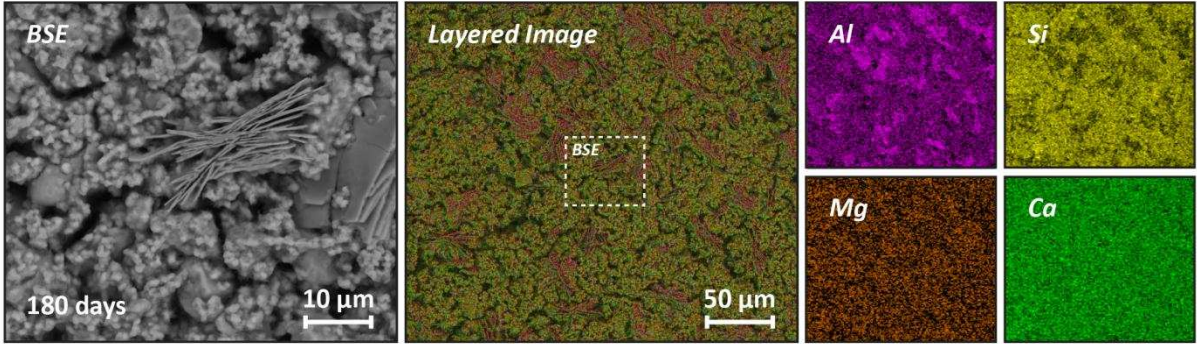
268 Crystals displaying a plate-like morphology and elemental composition characteristic of AFm-type  
269 phases [58] and hydrotalcite-group phases [6, 8] are also observed in the BSE images and elemental  
270 maps for samples D, E, J and K cured for 180 days (Figure 4 and Appendix B, Supporting Information).  
271 The Mc phase identified by XRD (Figure 1) is observed most prominently in elemental maps of  
272 sample D at all ages, as an Al-rich, Si- and Na-deficient crystalline phase containing a level of calcium  
273 which is not discernible from that of the surrounding C-(A)-S-H (Figure 4). A Ca-rich phase exhibiting  
274 a plate-like morphology characteristic of portlandite [59] is observed in samples H-L at all ages  
275 (Figure 5 and Figure S6 - S9, Supporting Information), again consistent with X-ray diffraction data for  
276 these samples. A representative BSE image exhibiting this phase is shown for sample L cured 180  
277 days (Figure 5).

278 Some small ( $< 2 \mu\text{m}$ ) plate-like crystals can be seen in the BSE images of samples D - L cured for 180  
279 days (shown for sample L in Figure 7). It is not possible to resolve the elemental composition of  
280 these crystals by EDX as their size is less than the depth of X-ray generation for the 15 keV  
281 accelerating voltage used [60], and consequently they are not distinguishable from the C-(A)-S-H  
282 phase when elemental maps are examined. However, these crystals exhibit morphology similar to  
283 the hydrotalcite-group phases identified in alkali-activated slag cements produced using slags  
284 containing approximately 8 wt. % MgO [6, 8]. No phases exhibiting distinct crystal habits can be  
285 seen in the BSE image of samples A, B and C.



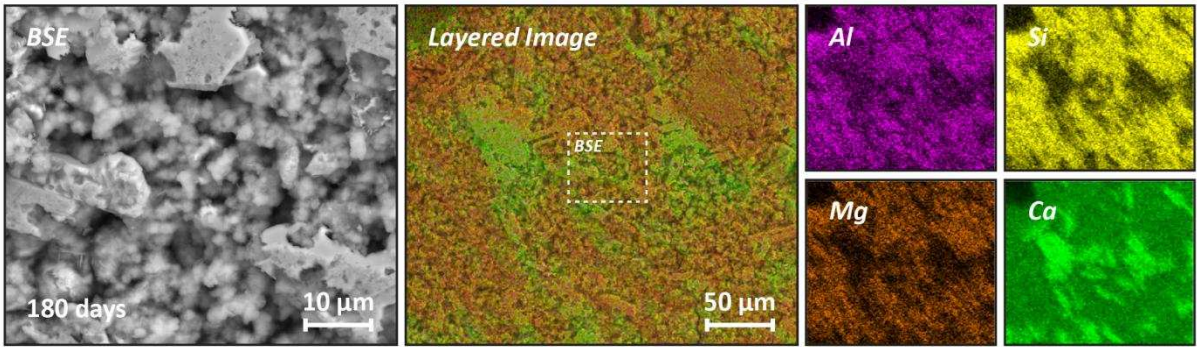
286

287 **Figure 3:** ESEM back-scattered electron (BSE) images and elemental maps of alkali-activated sample A cured for 180 days



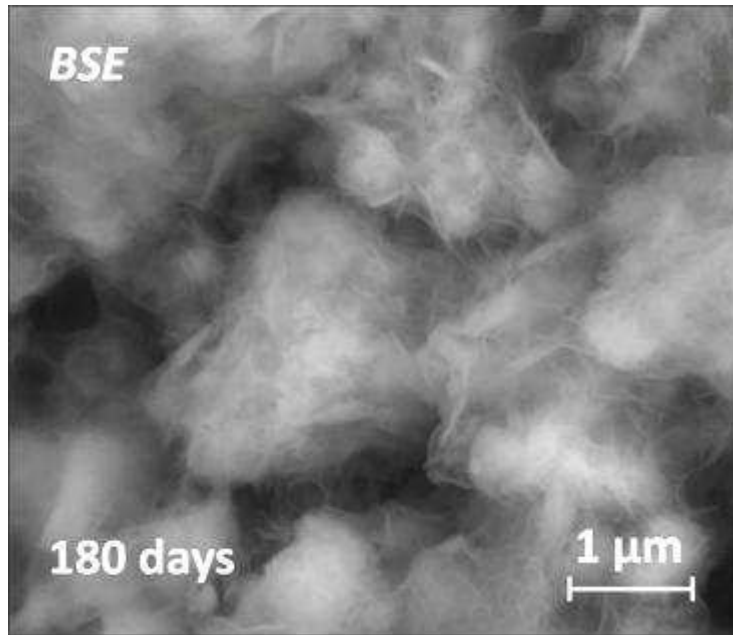
288

289 **Figure 4:** ESEM back-scattered electron (BSE) images and elemental maps of alkali-activated sample D cured for 180 days



290

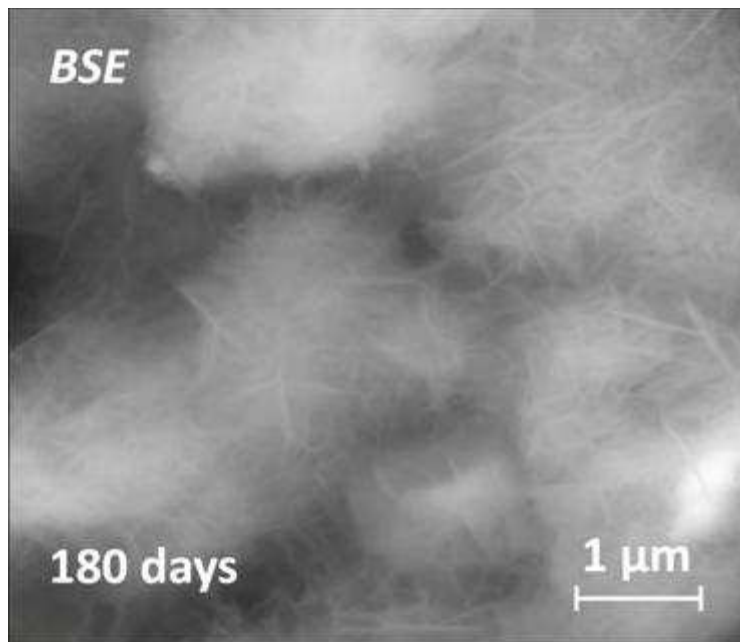
291 **Figure 5:** ESEM back-scattered electron (BSE) images and elemental maps of alkali-activated sample L cured for 180 days



292

293 **Figure 6:** Back-scattered electron (BSE) image of alkali-activated sample L cured for 180 days showing the globular, fibrous  
294 morphology of the C-(A)-S-H gel

295



296

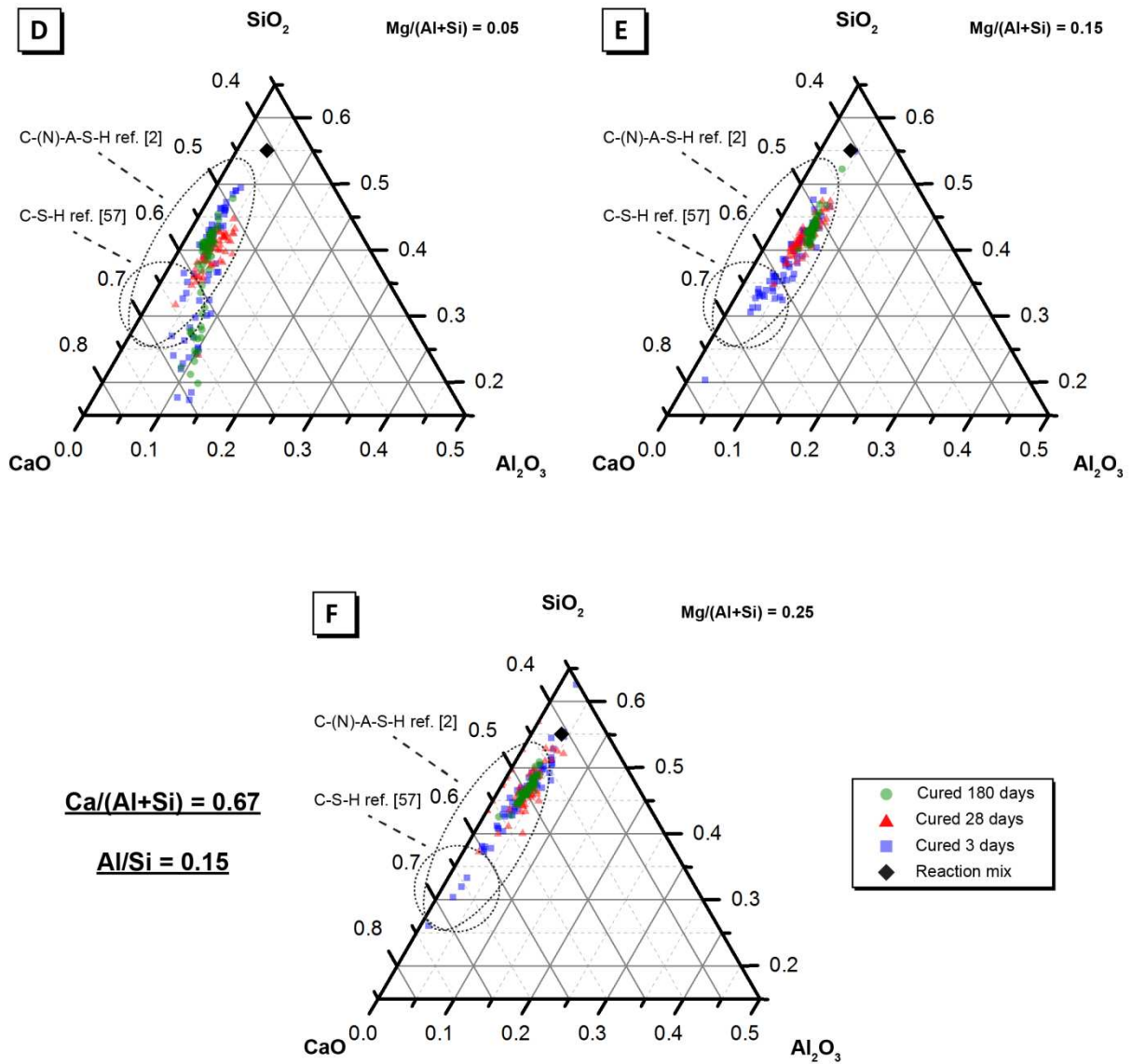
297 **Figure 7:** Back-scattered electron (BSE) image of alkali-activated sample L cured for 180 days showing plate-like crystals  
298 exhibiting morphology similar to hydrotalcite-group phases, amongst C-(A)-S-H gel

299

300 The elemental compositions of each ESEM-EDX spot analysis conducted on each sample, projected  
301 onto the  $\text{CaO-Al}_2\text{O}_3\text{-SiO}_2$  ternary system, are reported in Figure 8 and Figure S10 - S13, Supporting  
302 Information. These data reveal important compositional changes induced by differences in reaction  
303 mix chemistry.

304 AAM samples A, B and C ( $\text{Ca}/(\text{Al}+\text{Si}) = 0.67$ ,  $\text{Al}/\text{Si} = 0.05$ ) exhibit a composition falling within regions  
305 commonly attributed to moderate-Ca ( $0.4 < \text{Ca}/\text{Si} < 0.5$ ) C-(N)-A-S-H and C-S-H gels in alkali-activated  
306 slag and slag/fly ash blends [61, 62] and in synthetic AAMs [17, 23, 36] (Figure S10, Supporting  
307 Information). Increased bulk Al content in sample D ( $\text{Ca}/(\text{Al}+\text{Si}) = 0.67$ ,  $\text{Al}/\text{Si} = 0.15$ ,  $\text{Mg}/(\text{Al}+\text{Si}) =$   
308  $0.05$ ) results in a composition within regions commonly attributed to a C-(N)-A-S-H gel, clustered  
309 along an imaginary line drawn between this region and AFm-type phases (Figure 8 and Figure S11,  
310 Supporting Information), consistent with the X-ray diffractograms for this sample (Figure 1).  
311 Increased bulk Al content in samples E and F ( $\text{Ca}/(\text{Al}+\text{Si}) = 0.67$ ,  $\text{Al}/\text{Si} = 0.15$ ,  $\text{Mg}/(\text{Al}+\text{Si}) = 0.15$  and  
312  $0.25$  respectively) does not result in compositions corresponding to AFm-type phases, indicating that  
313 increased Mg content of these samples inhibits the formation of these phases. This is consistent with  
314 the trends observed by XRD, where increased precursor bulk Mg content promotes formation of  
315 gehlenite during precursor synthesis and calcination, consequently decreasing the amount of 'freely  
316 available' aluminium within the glassy phase of the precursors and inhibiting the formation of AFm-  
317 type phases upon alkali-activation.

318



319

320 **Figure 8:** Projection of alkali-activated material chemistry onto the ternary CaO – Al<sub>2</sub>O<sub>3</sub> – SiO<sub>2</sub> system (neglecting Na<sub>2</sub>O and  
 321 MgO content) showing elemental composition of AAMs cured for 3, 28 and 180 days for samples D, E and F (Ca/(Al+Si) =  
 322 0.67 and Al/Si = 0.15) as marked, as determined by ESEM-EDX analysis. A random selection of points evenly distributed  
 323 across a representative 500 μm × 500 μm section of the sample were used for analysis, with an interaction volume of  
 324 approximately 2μm<sup>3</sup> [63]. Approximate regions of C-S-H and C-(N)-A-S-H determined from [2] and [62]. Ternary CaO – Al<sub>2</sub>O<sub>3</sub>  
 325 – SiO<sub>2</sub>, MgO – Al<sub>2</sub>O<sub>3</sub> – SiO<sub>2</sub> and Na<sub>2</sub>O – Al<sub>2</sub>O<sub>3</sub> – SiO<sub>2</sub> diagrams for all other samples are provided in Appendix B, Supporting  
 326 Information.

327

328 AAM samples G, H and I ( $\text{Ca}/(\text{Al}+\text{Si}) = 1.00$ ,  $\text{Al}/\text{Si} = 0.05$ ) exhibit a composition within regions  
329 commonly attributed to high-Ca ( $0.5 < \text{Ca}/\text{Si} < 0.6$ ) C-(N)-A-S-H and C-S-H gels (Figure S12, Supporting  
330 Information). Increased bulk Al content in sample J, K and L ( $\text{Ca}/(\text{Al}+\text{Si}) = 1.00$ ,  $\text{Al}/\text{Si} = 0.15$ ) does not  
331 result in compositions corresponding to AFm-type phases (Figure S13, Supporting Information),  
332 indicating that with high bulk Al content and sufficient Mg content ( $\text{Mg}/(\text{Al}+\text{Si}) = 0.05$ ) formation of  
333 Mg-containing LDH phases (e.g. hydroxalite-group phases) is preferred to Mg-free LDH phases (e.g.  
334 Mc). The portlandite identified in the X-ray diffractograms for samples B, C and H - L and is also  
335 evident by the compositions of these samples exhibited in Figures S10 and S12, respectively.

336 Among samples D, E and F ( $\text{Ca}/(\text{Al}+\text{Si}) = 0.67$ ,  $\text{Al}/\text{Si} = 0.15$ , varying Mg content), increased bulk Mg  
337 content in the precursor powder promotes greater formation of C-(N)-(A)-S-H and less formation of  
338 C-S-H and AFm-type phases, consistent with the XRD data in Figure 1. Increased precursor bulk Mg  
339 content at this composition causes formation of åkermanite and thus restricts the availability of Mg  
340 for alkali-activation reactions. Consequently, more Al is available to substitute into the C-(N)-A-S-H  
341 gel framework during gel formation.

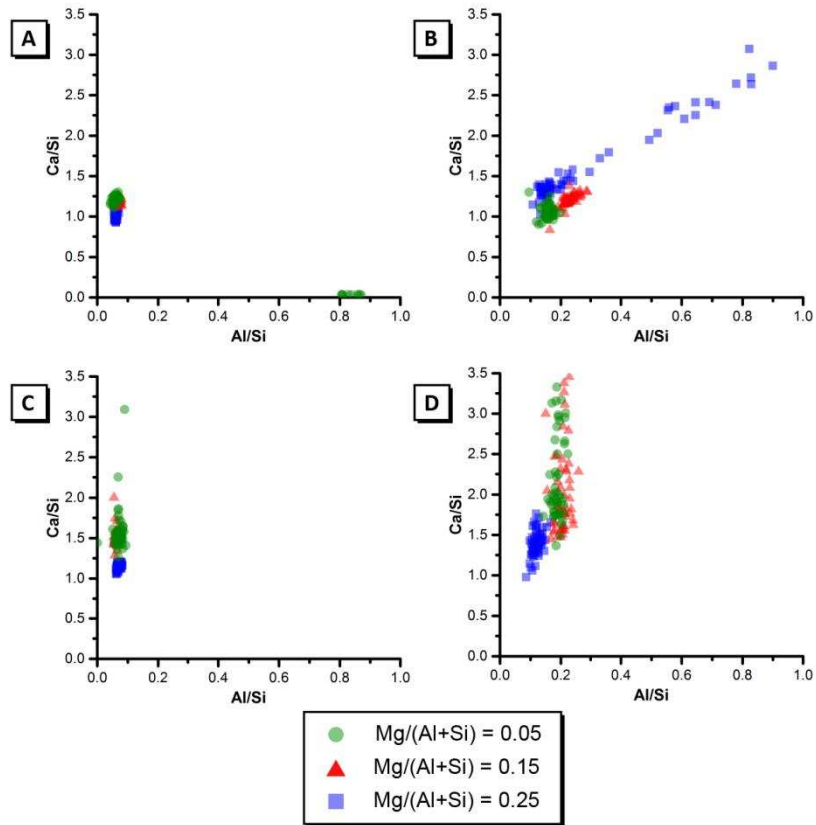
342 However, the converse is observed when examining samples J, K and L ( $\text{Ca}/(\text{Al}+\text{Si}) = 1.00$ ,  $\text{Al}/\text{Si} =$   
343  $0.15$ , carrying Mg content). Among these samples, increased bulk Mg content promotes formation of  
344 high-Ca C-S-H and portlandite, as the formation of åkermanite and gehlenite in the precursor  
345 powders is much less prominent at this higher Ca content. The Mg in these samples thus reacts (and  
346 consumes Al) to form hydroxalite-group phases, and consequently less Al is available to substitute  
347 into the C-S-H gel. Thus, in addition to the bulk magnesium content of the precursor, its disposition  
348 within the calcined powders also plays a very significant role in determining the hydrated phase  
349 assemblages in these alkali-activated materials.

350 These trends correlate well with those observed for alkali-activated slag binders, where reduced Al  
351 uptake by C-S-H was observed when using slags with higher bulk MgO content [8, 10]. All slags used  
352 within these studies contain åkermanite, with the exception of one low-MgO slag (1.17 wt. % MgO)  
353 [10], and consequently bulk MgO content cannot be used as a singular parameter to predict phase  
354 assemblage of Mg-containing additional reaction products.

355 Increasing precursor Mg content within all samples results in formation of reaction products  
356 exhibiting compositions within regions attributed to high-Ca ( $0.5 < \text{Ca/Si} < 0.6$ ) C-(N)-A-S-H and C-S-H  
357 gels (again due to increased amounts of åkermanite and hydrotalcite-group phases reducing the  
358 amount of Al in the glassy phase of the precursors). Increased bulk Ca content in the initial  
359 precursors for all samples results in a shift in sample composition towards Ca-rich C-(N)-A-S-H and C-  
360 S-H gels, consistent with observations for Mg-free synthetic AAM [36] and indicating that the Ca  
361 content of these gels is not influenced by bulk Mg content in any appreciable way.

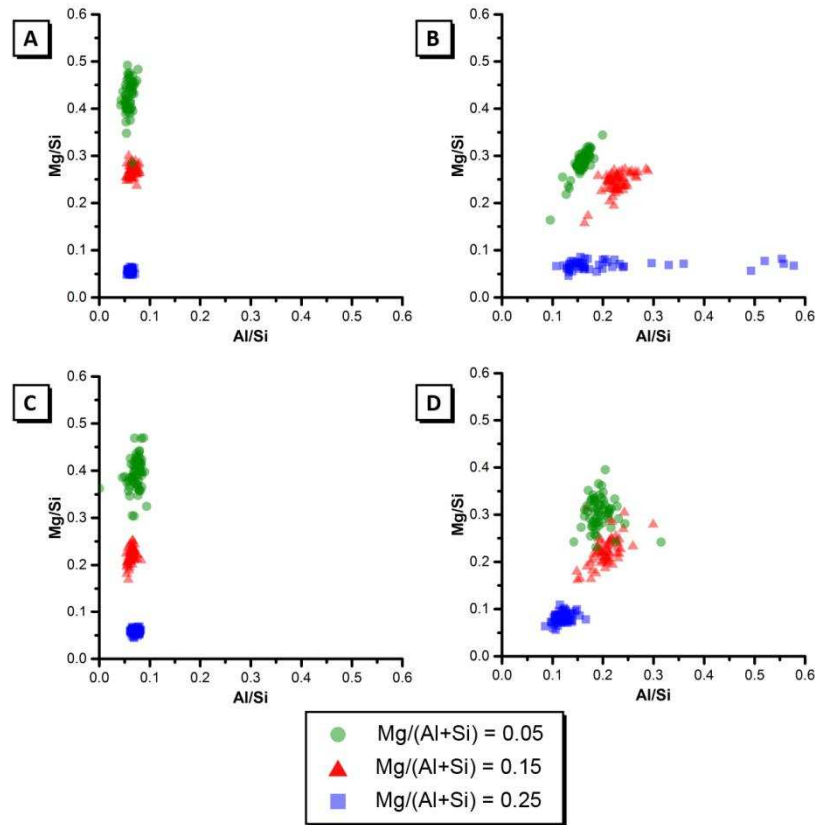
362 Each AAM exhibits  $\text{Mg}/(\text{Al}+\text{Si})$  ratios clustered along an imaginary line drawn between the  
363 composition of the precursor and the composition of hydrotalcite group phases (Figures S14 - S17,  
364 Supporting Information), heavily weighted towards the composition of the precursor. The  
365 composition of the hydrotalcite group phase with which the cluster of  $\text{Mg}/(\text{Al}+\text{Si})$  ratio data points  
366 align is dependent on precursor Mg content, with increased Mg content causing the cluster to align  
367 with a hydrotalcite group phase with  $\text{Mg}/\text{Al} \approx 5.2$  and decreased Mg content causing the cluster to  
368 align with a hydrotalcite group phase with  $\text{Mg}/\text{Al} \approx 1.2$ .

369 Changes in the Ca/Si, Al/Si and Mg/Si ratios of the binders cured for 180 days were also determined  
370 by ESEM-EDX, and are shown in Figure 9 and Figure 10 (changes in the Ca/Si, Al/Si and Mg/Si ratios  
371 of the binders as a function of curing time (determined by ESEM-EDX) are shown in Figure S22 and  
372 S23, Supporting Information). Each AAM displays a range of values for the ratios Ca/Si, Mg/Si and  
373 Al/Si which are similar to those observed for alkali silicate-activated GGBFS slags where the  
374 precursor slag contained between 1.17, and 13.2 wt % MgO [6, 8-10, 27]. This suggests that the  
375 chemistry of these binders produced from synthetic slags is generally representative of that of alkali  
376 silicate-activated commercial slags with varying magnesium content.



377

378 **Figure 9:** Summary of bulk atomic ratios Ca/Si versus Si/Al (60 measurements per sample) for the alkali-activated material  
 379 cured for 180 days for samples a) A, B and C ( $\text{Ca}/(\text{Al}+\text{Si}) = 0.67$ ,  $\text{Al}/\text{Si} = 0.05$ ), b) D, E and F ( $\text{Ca}/(\text{Al}+\text{Si}) = 0.67$ ,  $\text{Al}/\text{Si} = 0.15$ ), c)  
 380 G, H and I ( $\text{Ca}/(\text{Al}+\text{Si}) = 1.00$ ,  $\text{Al}/\text{Si} = 0.05$ ) and d) J, K and L ( $\text{Ca}/(\text{Al}+\text{Si}) = 1.00$ ,  $\text{Al}/\text{Si} = 0.15$ ), with  $\text{Mg}/(\text{Al}+\text{Si})$  ratios as  
 381 indicated.



382

383 **Figure 10:** Summary of bulk atomic ratios Mg/Si versus Si/Al (60 measurements per sample) for the alkali-activated  
 384 material cured for 180 days for samples a) A, B and C ( $\text{Ca}/(\text{Al}+\text{Si}) = 0.67$ ,  $\text{Al}/\text{Si} = 0.05$ ), b) D, E and F ( $\text{Ca}/(\text{Al}+\text{Si}) = 0.67$ ,  $\text{Al}/\text{Si} =$   
 385  $0.15$ ), c) G, H and I ( $\text{Ca}/(\text{Al}+\text{Si}) = 1.00$ ,  $\text{Al}/\text{Si} = 0.05$ ) and d) J, K and L ( $\text{Ca}/(\text{Al}+\text{Si}) = 1.00$ ,  $\text{Al}/\text{Si} = 0.15$ ), with  $\text{Mg}/(\text{Al}+\text{Si})$  ratios as  
 386 indicated.

387 The Al/Si ratios of low-Al AAM samples A, B, and C ( $\text{Ca}/(\text{Al}+\text{Si}) = 0.67$ ,  $\text{Al}/\text{Si} = 0.05$ ) and G, H, I  
 388 ( $\text{Ca}/(\text{Al}+\text{Si}) = 1.00$ ,  $\text{Al}/\text{Si} = 0.05$ ) remain generally constant at all ages, however the Ca/Si ratios shift  
 389 toward lower values and become more tightly clustered with increased curing time (Figure S22,  
 390 Supporting Information). This is attributed to slower dissolution of Si from the precursor and thus  
 391 increased incorporation of Si in the C-(N)-A-S-H gel as the reaction progresses. Low-Ca, high-Al AAM  
 392 samples D, E, and F ( $\text{Ca}/(\text{Al}+\text{Si}) = 0.67$ ,  $\text{Al}/\text{Si} = 0.15$ ) exhibit much wider ranges of Al/Si ratios due to  
 393 the presence of AFm-type phases (Figure 9 and Figure S22, Supporting Information), although the  
 394 degree of variability is reduced with increasing bulk Mg content, as increased formation of  
 395 hydrotalcite-group phases likely reduces the amount of Al available for AFm formation.

396 Such a trend is not observed for high-Ca, high-Al samples J, K, and L ( $\text{Ca}/(\text{Al}+\text{Si}) = 1.00$ ,  $\text{Al}/\text{Si} = 0.15$ ).  
 397 Al/Si ratios for these samples are clustered around that of the stoichiometric design, with little

398 variation in Al/Si ratio as bulk Mg content is varied (Figure S23, Supporting Information). These  
399 samples exhibit a large range of Ca/Si ratios (approximately  $1 < \text{Ca/Si} < 3$  in spot analyses), which can  
400 in part be attributed to the presence of portlandite in these samples (Figure 1); the same holds for  
401 the high-Ca, low-Al samples G, H, and I ( $\text{Ca}/(\text{Al}+\text{Si}) = 1.00$ ,  $\text{Al}/\text{Si} = 0.05$ ).

402 The correlation of Mg/Si with Al/Si ratios for each sample in Figure 10 is broadly consistent with the  
403 observation of hydrotalcite-group phases in the X-ray diffractograms (Figure 1) [3, 19]. The Mg/Al  
404 ratio of the hydrotalcite-group phases present in cementitious binders is often estimated (assuming  
405 the absence of other Mg-containing phases, or intermixed aluminate phases such as AFm) from the  
406 slope of a trendline drawn on the Mg/Si vs Al/Si plot [3, 19]. For the samples analysed here, these  
407 ratios range between 1.26 (sample G cured 3 days) and 5.21 (sample C cured 3 days) (Figure S23,  
408 Supporting Information). This range of values is much broader than the known range of Mg/Al values  
409 in hydrotalcite-group minerals [64]. The Mg/Al ratios calculated by this method for the samples with  
410 high bulk Mg content (samples C, F, I and L) are significantly higher than that of true hydrotalcite  
411 ( $\text{Mg}_6\text{Al}_2\text{CO}_3(\text{OH})_{16}\cdot 4\text{H}_2\text{O}$ ). This increases further in samples with low bulk Al content (samples F and  
412 L), indicating the possible presence of an additional Mg-rich phase in these samples, potentially a  
413 disordered magnesium silicate as crystalline brucite is not observed by XRD.

414 In all samples, when  $\text{Ca}/(\text{Al}+\text{Si})$  and  $\text{Al}/\text{Si}$  ratios are held constant, increasing precursor bulk Mg  
415 content appears from the trendline slopes to promote formation of hydrotalcite-group phases with  
416 higher Mg/Al ratios (Figure 10 and Figure S23, Supporting Information). However, the slopes of the  
417 trendlines correlating Mg/Si and Al/Si ratios for samples D and J are not consistent with the known  
418 chemistry of hydrotalcite-group phases, due to the formation of AFm-type phases as identified by  
419 XRD (Figure 1). Similar trends can be observed by examining previously published SEM-EDX data for  
420 alkali-activated slag cements produced from slags containing varying MgO contents [6, 8, 10]. When  
421 the  $\text{Mg}/(\text{Al}+\text{Si})$  and  $\text{Al}/\text{Si}$  ratios are held constant, an increased  $\text{Ca}/(\text{Al}+\text{Si})$  ratio does not change the  
422 Mg/Al ratio of the hydrotalcite-group phases.

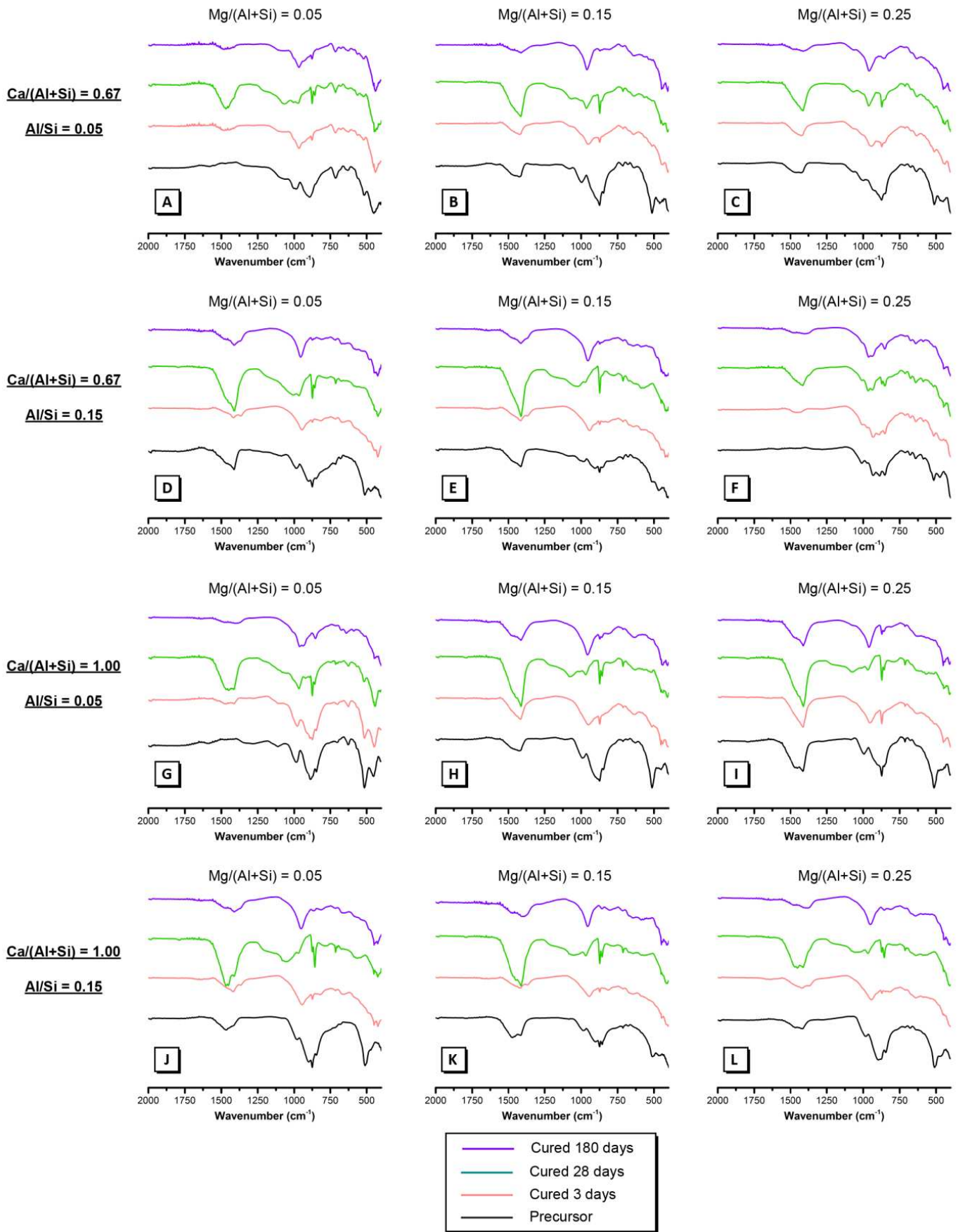
423

424

### 425 *3.4 Attenuated total reflectance Fourier transform infrared spectroscopy*

426 ATR-FTIR spectra collected for the AAMs are presented in Figure 11; full interpretation of ATR-FTIR  
427 spectra of the precursors is provided in Appendix C, Supporting Information. Alkali-activation  
428 produces a broad intense band at approximately  $970\text{ cm}^{-1}$  in the spectra of all samples cured for 3  
429 days, attributed to asymmetric stretching vibrations of Si-O-T bonds (T: tetrahedral Si or Al) in the  
430 chain structure of C-(A)-S-H [16, 65]. This band sharpens as curing time increases, indicating that  
431 greater structural ordering of C-(A)-S-H evolves as the reaction proceeds. Increased curing time also  
432 sees a shift in this band to slightly higher wavenumbers in the spectra for all samples by 28 days, and  
433 then a shift to lower wavenumbers by 180 days. This indicates increased polymerisation and  
434 crosslinking of C-(A)-S-H between 3 and 28 days via condensation of tetrahedral species, followed by  
435 increased inclusion of Al within the C-(A)-S-H gel between 28 and 180 days [52, 61]. The sharp band  
436 at  $875\text{ cm}^{-1}$  in the spectra of all AAMs at all ages is associated with asymmetric stretching of  $\text{AlO}_4^-$   
437 groups in Al-O-Si bonds within the C-(A)-S-H gel [66], however some intensity of this band is likely to  
438 be due to similar environments within remnant precursor particles (Appendix C, Supporting  
439 Information).

440 Samples with higher bulk Mg content exhibit the lowest wavenumbers for the band associated with  
441 Si-O-T bonds in the chain structure of C-(A)-S-H after 180 days of curing, indicating that these  
442 samples exhibit greater long term polymerisation and crosslinking of the C-(A)-S-H gel. The reduction  
443 in hydrotalcite-group phase formation in these samples discussed in section 3.1 results in increased  
444 availability of Al to participate in this process. The correlation between increased Al content and  
445 increased polymerisation and crosslinking of C-(A)-S-H is consistent with the results of  
446 thermodynamic modelling of sodium silicate-activated slag systems [2], and has also been observed  
447 experimentally in synthetic AAMs [36]; the trends identified here show the mechanisms through  
448 which MgO availability controls C-(A)-S-H gel composition and nanostructure.



450 **Figure 11:** ATR-FTIR spectra of the precursor powder and alkali-activated material for samples A – L cured for 3, 28 and 180  
 451 days as indicated

## 452 3.5 Solid state magic angle spinning nuclear magnetic resonance

### 453 3.5.1 $^{27}\text{Al}$ MAS NMR

454 The  $^{27}\text{Al}$  MAS NMR spectra of the precursors and AAMs for each sample are presented in Figure 12.  
455 The spectra of each of the precursors are very similar, the main feature being a broad tetrahedral  
456  $\text{AlO}_4$  resonance centred at approximately 57 ppm. Another broad tetrahedral  $\text{AlO}_4$  resonance is  
457 observed at approximately 74 ppm in low Ca ( $\text{Ca}/(\text{Al}+\text{Si}) = 0.67$ ) samples and at approximately 84  
458 ppm in high Ca samples ( $\text{Ca}/(\text{Al}+\text{Si}) = 0.67$ ). This resonance increases in intensity with increasing  
459  $\text{Mg}/(\text{Al}+\text{Si})$  ratio. These tetrahedral resonances are attributed to a distribution of Al environments  
460 within the glassy phase of the precursor (as identified by XRD), similar to that observed for GGBFS  
461 [10, 29]. The increased intensity of the  $\text{Al}^{\text{IV}}$  resonance at higher frequency is attributed to the  
462 gehlenite present in the higher-Mg precursors.

463 The spectra of each precursor display low intensity resonances centred at approximately 11 ppm and  
464 -3 ppm, each attributed to octahedral  $\text{AlO}_6$  environments. The intensity of the resonance at 11 ppm  
465 varies between samples and is assigned to the tricalcium aluminate phase [67] (consistent with that  
466 identified by XRD in some precursors), while the resonance at -3 ppm is attributed to  $\text{Al}^{\text{VI}}$  linked to  
467 Mg in a spinel-type structure [68].

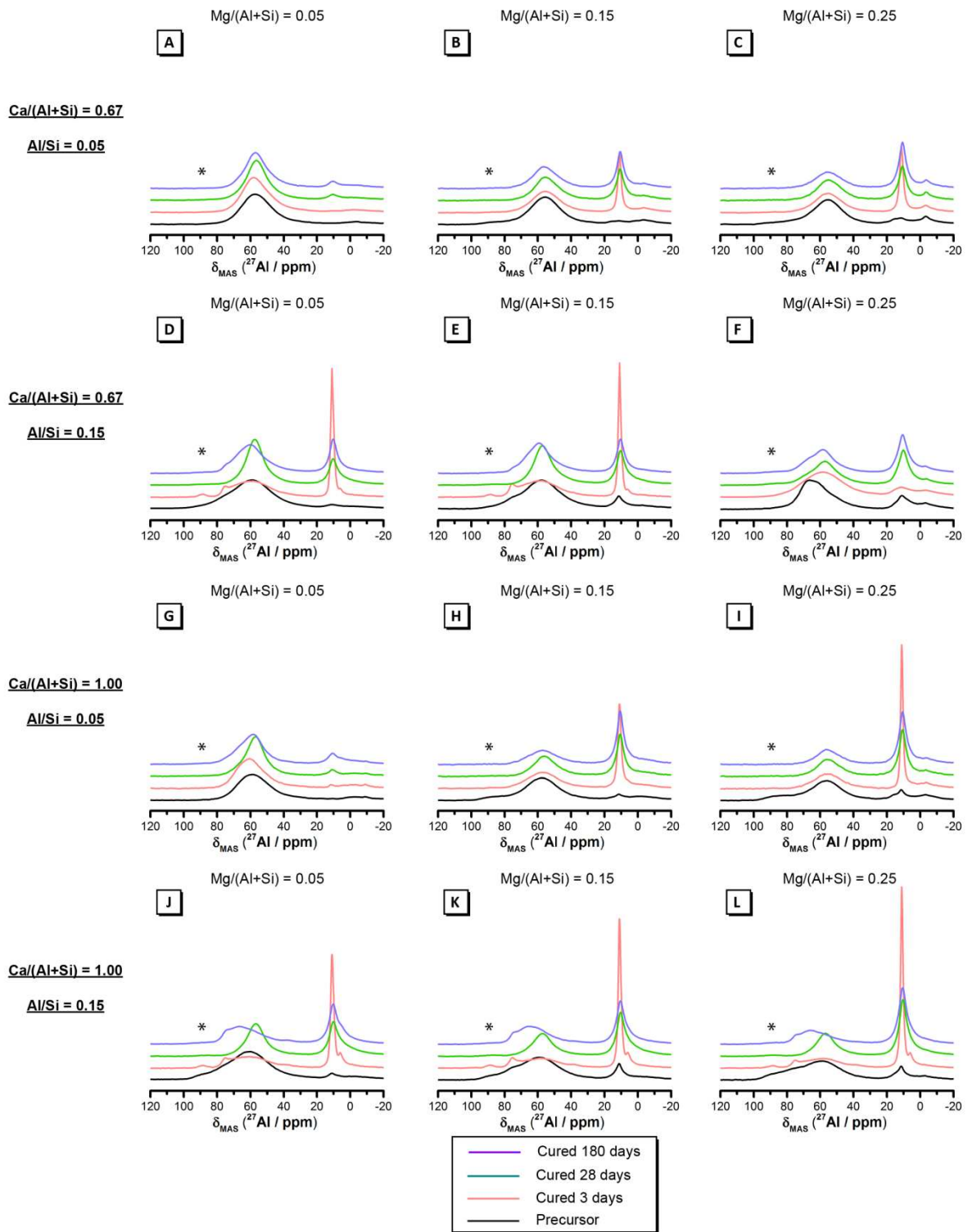
468 The  $^{27}\text{Al}$  MAS NMR spectra of each AAM cured for 3 days display a low intensity broad resonance  
469 spanning from 35 ppm to 75 ppm with a maximum at approximately 58 ppm; this is assigned to Al in  
470 a significantly distorted tetrahedral environment [27, 29, 69]. A low intensity narrow resonance at  
471  $\sim 76$  ppm assigned to Al in a well defined tetrahedral coordination is also observed in the spectra of  
472 the AAMs for samples D, E, J, K and L. Well-ordered C-(N)-A-S-H identified in the AAMs for each of  
473 these samples by XRD and ESEM-EDX will contain tetrahedral Al substituted for Si bridging sites,  
474 leading to the well defined resonance observed at 76 ppm [30, 32, 70], while poorly crystalline C-(N)-  
475 A-S-H and amorphous N-A-S-H will contain Al in significantly distorted tetrahedral environments,  
476 leading to the broad resonance centred at approximately 58 ppm. The narrow resonance at

477 approximately 11 ppm in all samples is assigned to Al in a well defined octahedral coordination  
478 within both AFm reaction products [69, 71] and hydrotalcite-group phases [25, 27, 72].

479 The resonance due to distorted Al<sup>IV</sup> environments shifts to lower chemical shift values between 3  
480 and 28 days, and back to higher chemical shift values between 28 and 180 days, consistent with  
481 observations by FTIR (section 3.4) of increased polymerisation of the C-(N)-A-S-H gel and a decrease  
482 in gel Ca/Si ratio between 3 and 28 days followed by increased Al incorporation in the C-(N)-A-S-H  
483 gel between 28 and 180 days. This is in contrast to observations of C-(N)-A-S-H gel evolution in Mg-  
484 free synthetic calcium aluminosilicate gels [36], where increased Al incorporation within the C-(N)-  
485 (A)-S-H gel was observed at early age due to the higher availability of this element for incorporation  
486 into the C-(N)-(A)-S-H in the absence of Mg. This is most pronounced for AAMs produced from  
487 precursors with low but non-zero bulk Mg content (which experienced the greatest formation of  
488 hydrotalcite-group phases, section 3.1).

489 The peak assigned to Al<sup>VI</sup> in AFm and hydrotalcite-group phases broadens between 3 and 28 days  
490 and remains unaltered thereafter. This suggests formation of very ordered AFm and hydrotalcite-  
491 group phases during the early stages of reaction due to high contents of available Al and Mg, and  
492 decreased ordering of these phases at later ages as interlayer carbonate incorporation begins.

493 A small resonance at 6 ppm is also observed in samples D, E, J, K and L and attributed to Al<sup>VI</sup> species  
494 within the 'third aluminate hydrate' (TAH), an amorphous nanoscale aluminate hydrate phase  
495 precipitated at the surface of the C-S-H type gels [71, 73], and which has also been noted in alkali-  
496 activated slags [29, 69] and synthetic Mg-free AAMs [22]. The presence of TAH in samples J, K and L  
497 (Ca/(Al+Si)=1.00) is consistent with stoichiometric arguments and thermodynamic modelling which  
498 suggest that the presence of TAH is likely to be linked to high concentrations of available Ca and Al  
499 [11, 19, 74], and previous experimental observations for synthetic Mg-free AAMs [36]. The presence  
500 of TAH in samples D and E (Ca/(Al+Si)=0.67, Mg/(Al+Si) = 0.05 and 0.15, respectively) suggests that  
501 even in the presence of lower bulk Ca content, the formation of higher amounts of hydrotalcite-  
502 group phases is compatible with the formation of TAH.



504

505 **Figure 12:**  $^{27}\text{Al}$  MAS NMR spectra of the precursor powders A-L, and the respective alkali-activated materials cured for 3, 28  
 506 and 180 days as indicated. Positions at which spinning side bands are expected are indicated by \*.

507

### 508 3.5.2 <sup>29</sup>Si MAS NMR

509 The <sup>29</sup>Si MAS NMR spectra for the precursors and AAMs are presented in Figure 13. For each sample,  
510 the spectrum of the precursor exhibits a broad resonance centred at approximately -83 ppm.  
511 Network modifying cations alter the chemical shifts of Q<sup>n</sup>(*m*Al) species, particularly for more strongly  
512 polarising cations such as calcium [75, 76], which will cause additional overlap between the  
513 individual Q<sup>n</sup>(*m*Al) environments. The presence of Al(VI) species further complicates peak  
514 assignment in the <sup>29</sup>Si MAS NMR spectra [24].

515 Due to its broad nature, it is likely that this resonance contains contributions from multiple different  
516 Q<sup>n</sup>(*m*Al) environments, with Q<sup>1</sup>, Q<sup>2</sup> and Q<sup>3</sup> silicate species present in a depolymerised calcium silicate  
517 phase and Q<sup>4</sup>(*m*Al) (*m* = 1 – 4) species in a highly polymerised aluminosilicate phase (indicated by the  
518 low intensity broad resonance observed at -105 to -110 ppm), similar to those observed in Mg-free  
519 calcium aluminosilicate precursors synthesised using the same method [24]. Three sharp low-  
520 intensity resonances are observed at -72 ppm, -73.5 ppm and -84.5 ppm in the spectra of the  
521 precursors and are assigned to the silicon environments within gehlenite and åkermanite (-72 ppm  
522 and -73.5 ppm) [77, 78] and wollastonite (-84.5 ppm) [79]. The intensities of these resonances vary  
523 between precursor samples, consistent with the trends in the XRD reflections attributed to these  
524 phases (section 3.1). These resonances remain largely unchanged throughout the alkali activation  
525 reaction process. A resonance from Ca<sub>2</sub>SiO<sub>4</sub> (identified by XRD) is also expected to contribute to the  
526 overall spectra at approximately -71.4 ppm [80, 81].

527 Three resonances observed at approximately -77 ppm, -80 ppm and -83 ppm in the <sup>29</sup>Si MAS NMR  
528 spectra for the alkali-activated binders are assigned to Q<sup>1</sup>, Q<sup>2</sup>(1Al), and Q<sup>2</sup> environments,  
529 respectively, within the C-(N)-A-S-H gel [2, 19, 29, 38]. In general, these resonances are sharpest and  
530 most intense in samples with increased bulk Ca and Mg content, suggesting a correlation between  
531 these constituents and ordering of the C-(N)-A-S-H gel. A significant degree of crosslinking between  
532 C-(N)-A-S-H gel aluminosilicate chains is also occurring in each sample as evidenced by intensity in  
533 the Q<sup>3</sup> and Q<sup>3</sup>(1Al) regions (-85 to -95 ppm) [2]; this is greatest for samples with higher bulk Mg

534 content but lower Mg availability as discussed above, which thus have more Al available to  
535 substitute for Si within the C-(N)-A-S-H gel. This promotes crosslinking due to the preference of Al to  
536 be located in crosslinked and polymerised sites [2, 25]. Conversely, samples with more hydrotalcite-  
537 group phase formation exhibit less intensity in the  $Q^2(1Al)$  region of the  $^{29}Si$  MAS NMR spectra,  
538 corresponding to the competition between hydrotalcite-group phases and Al uptake in C-(N)-A-S-H  
539 [8, 10].

540 The low intensity broad resonance originally observed at approximately -110 ppm in the spectra of  
541 each calcined precursor powder remains mostly unaltered in the spectra of the alkali-activated  
542 binders produced from each of the respective precursors. It is possible that this is because the  
543 polymerised aluminosilicate phase in the precursor does not participate significantly during alkali-  
544 activation, however it is much more likely that  $Q^4(mAl)$  within a N-A-S-H gel that has formed as an  
545 additional reaction product are contributing to the intensity in this region of the spectra, as observed  
546 previously for synthetic Mg-free AAM [36].

547

548

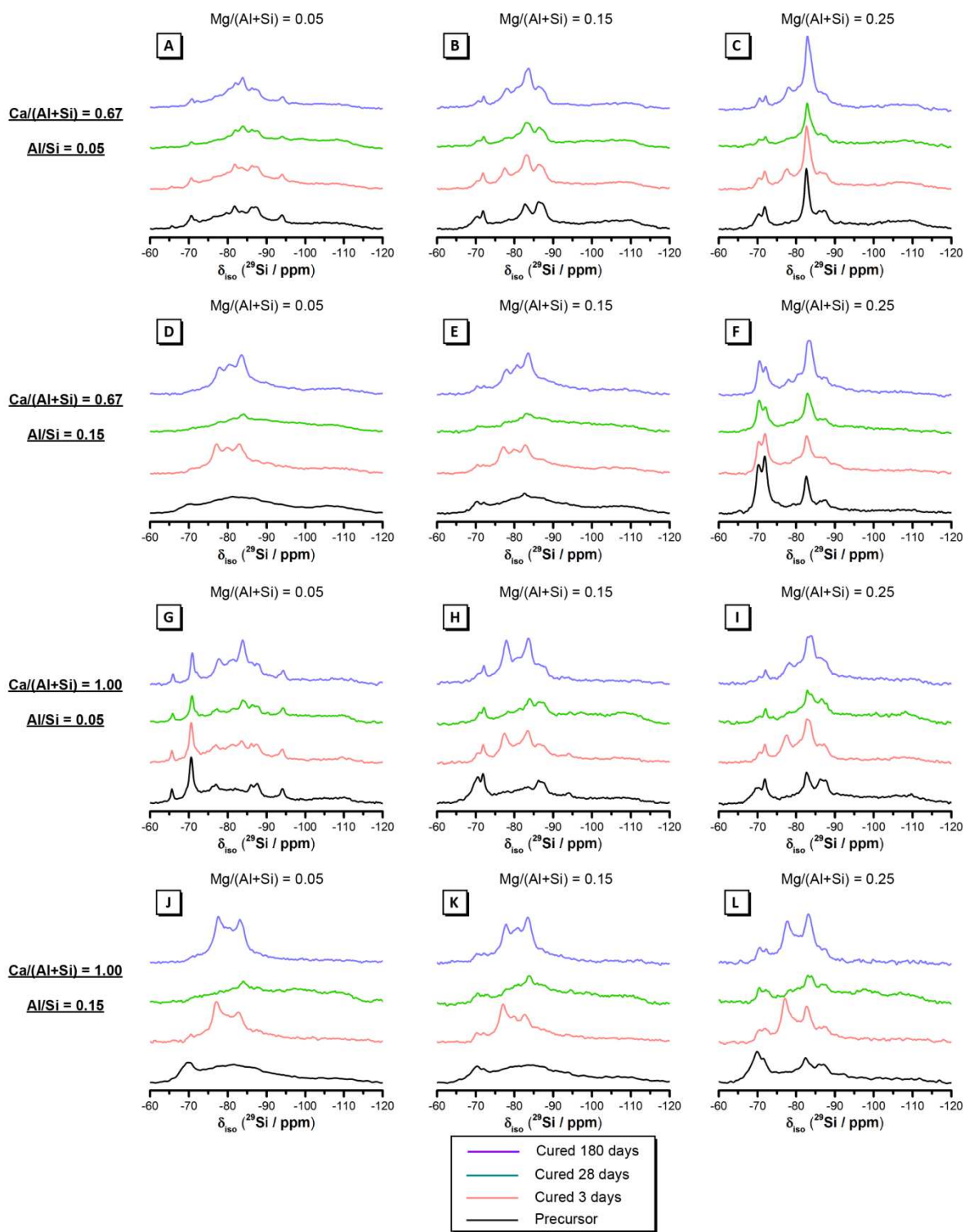


**Figure 13:**  $^{29}\text{Si}$  MAS NMR spectra of the precursor powders A-L, and the respective alkali-activated materials cured for 3, 28 and 180 days as indicated.

### 3.5.3 $^{23}\text{Na}$ MAS NMR

The  $^{23}\text{Na}$  MAS NMR spectra for each AAM exhibit a single broad resonance centred at approximately  $-0.2$  to  $-4.2$  ppm (Figure 14). This resonance is attributed to  $\text{Na}^+$  cations associated with aluminium-centred tetrahedra, playing a charge-balancing role within the C-(N)-A-S-H gel framework [69, 82].  $\text{Na}^+$  cations that are charge-balancing aluminium-centred tetrahedra in any N-A-S-H gel frameworks present (tentatively identified by  $^{29}\text{Si}$  MAS NMR, section 3.5.2) also contribute to the signal in this region [21, 48]. This resonance is observed in the spectra of each AAM at all ages, and shifts toward lower chemical shift at approximately  $-4.5$  ppm by 28 days before moving to higher chemical shift at approximately  $-2.5$  to  $-3.5$  ppm by 180 days. These shifts show variations in the electron density around the Na nuclei as the samples age, but do not correlate directly with changes in Mg content, suggesting that (as observed by  $^{23}\text{Na}$  MAS NMR) these changes in Mg content do not alter the local environment of the charge-balancing sodium ions. A broad, low intensity shoulder at approximately  $-16$  ppm is observed in the  $^{23}\text{Na}$  MAS NMR spectra of each sample, attributed to Na sorbed to the surfaces of the nanostructured gel [36]. The intensity of this resonance increases with increased bulk Mg content.

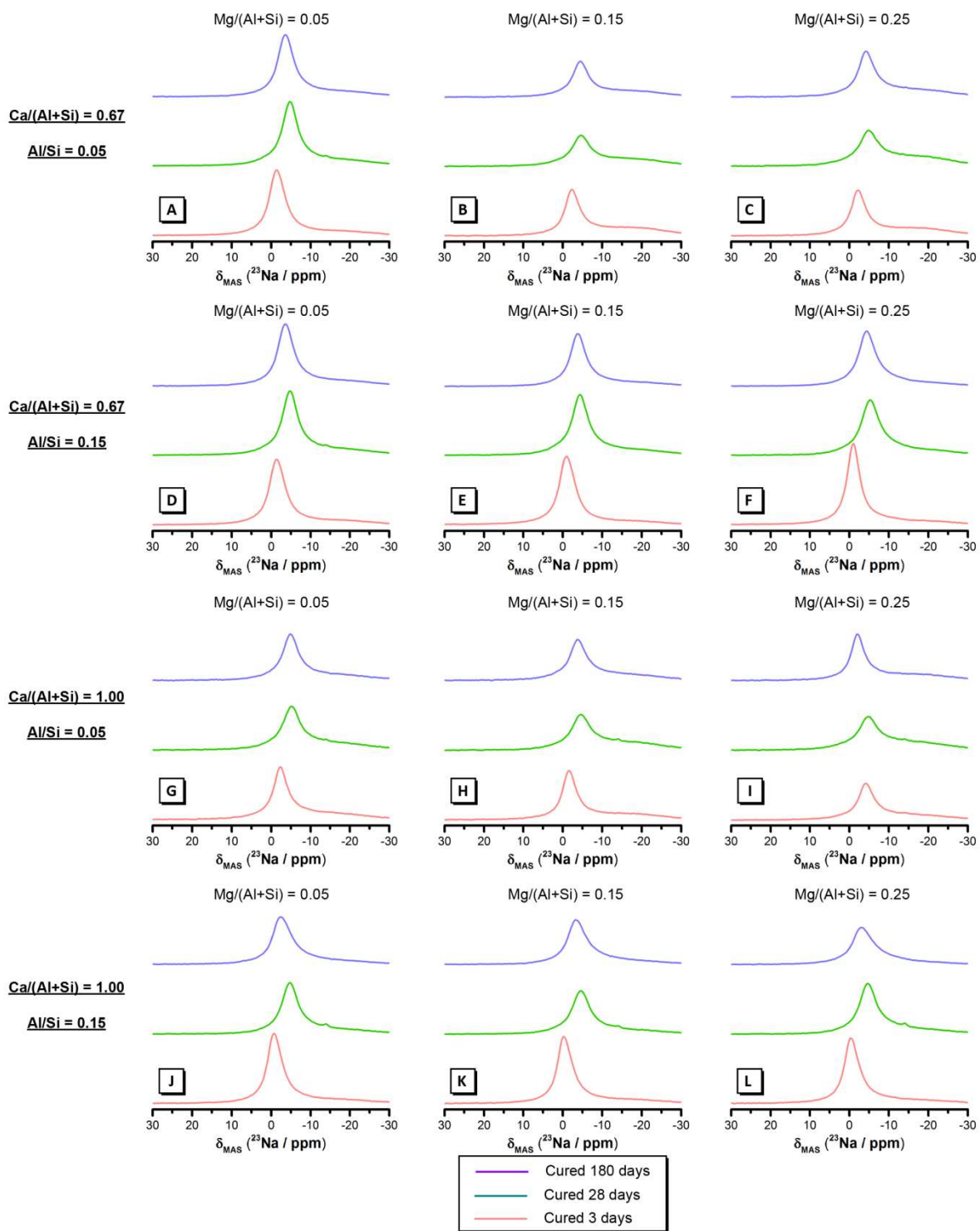


**Figure 14:**  $^{23}\text{Na}$  MAS NMR spectra of the precursor powders A-L, and the respective alkali-activated materials cured for 3, 28 and 180 days as indicated.

#### 4. Conclusions

Findings here show even small changes in reaction mixture Mg content can induce significant changes in phase formation and nanostructural development of AAM. Freely available Mg content (i.e. Mg present in glassy, reactive precursor species which is dissolved during alkali activation) controls the formation of hydrotalcite-group and AFm-type phases, which in turn strongly affect C-(N)-A-S-H gel chemistry and nanostructure. In the presence of high bulk Al content and sufficient Mg content ( $\text{Mg}/(\text{Al}+\text{Si}) = 0.05$ ) formation of Mg-containing LDH phases (e.g. hydrotalcite-group phases) is preferential to Mg-free LDH phases (e.g. Mc). A strong correlation between bulk Mg content and the Mg/Al ratio of hydrotalcite-group phases is observed, with increased Mg content resulting in higher Mg/Al ratios (up to  $\text{Mg}/\text{Al} \approx 5.2$ ) and decreased Mg content reducing the Mg/Al ratio of hydrotalcite-group phases to approximately  $\text{Mg}/\text{Al} \approx 1.2$ .

Decreased bulk Ca content inhibits formation of AFm-type additional reaction products, and increased precursor bulk Mg content causes formation of åkermanite and impedes formation of hydrotalcite-group phases due to less Mg available upon alkali-activation. Consequently more Al is then available to substitute into the C-(N)-A-S-H gel framework during gel formation. With sufficient Ca, increased bulk Mg promotes formation of low-Al C-(A)-S-H and portlandite, due to formation of hydrotalcite-group phases and a reduction in available Al. Hydrotalcite-group phase formation is linked to increased C-(N)-A-S-H gel polymerisation, decreased gel Al uptake and increased formation of the 'third aluminate hydrate'.

Through the use of pure systems parameters dictating phase evolution can be controlled, as demonstrated in this study, and can be used to identify and understand the physiochemical interactions occurring during alkali-activation of aluminosilicate precursors and subsequent formation of cementitious materials. This work highlights the importance of considering available chemical constituents rather than simply bulk composition, so that the desired binder structure for a particular application can be achieved.

## 5. Acknowledgements

This work has been funded by the Australian Research Council (ARC), including support through the Particulate Fluids Processing Centre, a Special Research Centre of the ARC. The University of Melbourne also provided support through an Overseas Research Experience Scholarship to support an extended visit by the first author to the University of Sheffield. We would like to acknowledge Ms Laura Jukes, Geopolymer and Minerals Processing Group, The University of Melbourne, for assistance with thermogravimetric analysis and laser granulometry experiments.

## References

- [1] J.L. Provis, A. Palomo, C. Shi, Advances in understanding alkali-activated materials, *Cem. Concr. Res.*, 78A (2015) 110-125.
- [2] R.J. Myers, S.A. Bernal, R. San Nicolas, J.L. Provis, Generalized structural description of calcium-sodium aluminosilicate hydrate gels: the cross-linked substituted tobermorite model, *Langmuir : the ACS journal of surfaces and colloids*, 29 (2013) 5294-5306.
- [3] I.G. Richardson, A.R. Brough, G.W. Groves, C.M. Dobson, The characterization of hardened alkali-activated blast-furnace slag pastes and the nature of the calcium silicate hydrate (C–S–H) paste, *Cement and Concrete Research*, 24 (1994) 813–829.
- [4] A. Fernández-Jiménez, F. Puertas, Structure of calcium silicate hydrates formed in alkaline-activated slag: Influence of the type of alkaline activator, *Journal of the American Ceramic Society*, 86 (2003) 1389-1394.
- [5] E. Douglas, A. Bilodeau, V.M. Malhotra, Properties and durability of alkali activated slag concrete, *Aci Mater J*, 89 (1992) 509-516.
- [6] M. Ben Haha, G. Le Saoût, F. Winnefeld, B. Lothenbach, Influence of activator type on hydration kinetics, hydrate assemblage and microstructural development of alkali activated blast-furnace slags, *Cement and Concrete Research*, 41 (2011) 301-310.
- [7] R.J. Myers, B. Lothenbach, S.A. Bernal, J.L. Provis, Thermodynamic modelling of alkali-activated slag cements, *Applied Geochemistry*, 61 (2015) 233-247.
- [8] M. Ben Haha, B. Lothenbach, G. Le Saoût, F. Winnefeld, Influence of slag chemistry on the hydration of alkali-activated blast-furnace slag — Part I: Effect of MgO, *Cement and Concrete Research*, 41 (2011) 955-963.

- [9] M. Ben Haha, B. Lothenbach, G. Le Saoût, F. Winnefeld, Influence of slag chemistry on the hydration of alkali-activated blast-furnace slag — Part II: Effect of  $\text{Al}_2\text{O}_3$ , Cement and Concrete Research, 42 (2012) 74-83.
- [10] S.A. Bernal, R. San Nicolas, R.J. Myers, R. Mejía de Gutiérrez, F. Puertas, J.S.J. van Deventer, J.L. Provis, MgO content of slag controls phase evolution and structural changes induced by accelerated carbonation in alkali-activated binders, Cement and Concrete Research, 57 (2014) 33-43.
- [11] J.L. Provis, J.S.J. van Deventer, Alkali Activated Materials. State-of-the-Art Report, RILEM TC 224-AAM, Springer2014.
- [12] S.A. Bernal, R. San Nicolas, J.L. Provis, R.M. de Gutierrez, J.S.J. van Deventer, Natural carbonation of aged alkali-activated slag concretes, Materials and Structures, 47 (2014) 693-707.
- [13] X. Ke, S.A. Bernal, J.L. Provis, Controlling the reaction kinetics of sodium carbonate-activated slag cements using calcined layered double hydroxides, Cement and Concrete Research, 81 (2016) 24-37.
- [14] X.-m. Cui, L.-p. Liu, G.-j. Zheng, R.-p. Wang, J.-p. Lu, Characterization of chemosynthetic  $\text{Al}_2\text{O}_3$ - $2\text{SiO}_2$  geopolymers, Journal of Non-Crystalline Solids, 356 (2010) 72-76.
- [15] I. García-Lodeiro, A. Fernández-Jimenez, A. Palomo, D.E. Macphee, Effect on fresh C-S-H gels of the simultaneous addition of alkali and aluminium, Cement and Concrete Research, 40 (2010) 27-32.
- [16] I. García-Lodeiro, A. Fernández-Jiménez, M.T. Blanco, A. Palomo, FTIR study of the sol-gel synthesis of cementitious gels: C-S-H and N-A-S-H, Journal of Sol-Gel Science and Technology, 45 (2008) 63-72.
- [17] I. García-Lodeiro, A. Palomo, A. Fernández-Jiménez, D.E. Macphee, Compatibility studies between N-A-S-H and C-A-S-H gels. Study in the ternary diagram  $\text{Na}_2\text{O}$ - $\text{CaO}$ - $\text{Al}_2\text{O}_3$ - $\text{SiO}_2$ - $\text{H}_2\text{O}$ , Cement and Concrete Research, 41 (2011) 923-931.
- [18] M. Gordon, J.L. Bell, W.M. Kriven, Comparison of naturally and synthetically-derived, potassium based geopolymers, Advances in Ceramic Matrix Composites X, John Wiley & Sons, Inc.2004, pp. 95-106.
- [19] S.-D. Wang, K.L. Scrivener,  $^{29}\text{Si}$  and  $^{27}\text{Al}$  NMR study of alkali-activated slag, Cement and Concrete Research, 33 (2003) 769-774.
- [20] S.-D. Wang, K.L. Scrivener, P.L. Pratt, Factors affecting the strength of alkali-activated slag, Cement and Concrete Research, 24 (1994) 1033-1043.
- [21] B. Walkley, R. San Nicolas, M.A. Sani, J.D. Gehman, J.S. van Deventer, J.L. Provis, Phase evolution of  $\text{Na}_2\text{O}$ - $\text{Al}_2\text{O}_3$ - $\text{SiO}_2$ - $\text{H}_2\text{O}$  gels in synthetic aluminosilicate binders, Dalton Transactions, 45 (2016) 5521-5535.
- [22] B. Walkley, R. San Nicolas, M.-A. Sani, G.J. Rees, J.V. Hanna, J.S.J. van Deventer, J.L. Provis, Phase evolution of C-(N)-A-S-H/N-A-S-H gel blends investigated via alkali-activation of synthetic calcium aluminosilicate precursors, Cement and Concrete Research, 89 (2016) 120-135.
- [23] B. Walkley, J.L. Provis, R. San Nicolas, M.A. Sani, J.S.J. van Deventer, Stoichiometrically controlled C-(A)-S-H/N-A-S-H gel blends via alkali-activation of synthetic precursors, Advances in Applied Ceramics, 114 (2015) 372-377.

- [24] B. Walkley, R. San Nicolas, M.A. Sani, J.D. Gehman, J.S.J. van Deventer, J.L. Provis, Synthesis of stoichiometrically controlled reactive aluminosilicate and calcium-aluminosilicate powders, *Powder Technology*, 297 (2016) 17-33.
- [25] R.J. Myers, S.A. Bernal, J.D. Gehman, J.S.J. van Deventer, J.L. Provis, The role of Al in cross-linking of alkali-activated slag cements, *Journal of the American Ceramic Society*, 98 (2015) 996-1004.
- [26] R.J. Myers, S.A. Bernal, J.L. Provis, A thermodynamic model for C-(N)-A-S-H gel: CNASH\_ss. Derivation and validation, *Cement and Concrete Research*, 66 (2014) 27-47.
- [27] G. Le Saoût, M. Ben Haha, F. Winnefeld, B. Lothenbach, C. Jantzen, Hydration degree of alkali-activated slags: A  $^{29}\text{Si}$  NMR study, *Journal of the American Ceramic Society*, 94 (2011) 4541-4547.
- [28] A.R. Brough, A. Atkinson, Sodium silicate-based, alkali-activated slag mortars Part I. Strength, hydration and microstructure, *Cement and Concrete Research*, 32 (2002) 865-879.
- [29] S.A. Bernal, J.L. Provis, B. Walkley, R. San Nicolas, J.D. Gehman, D.G. Brice, A.R. Kilcullen, P. Duxson, J.S.J. van Deventer, Gel nanostructure in alkali-activated binders based on slag and fly ash, and effects of accelerated carbonation, *Cement and Concrete Research*, 53 (2013) 127-144.
- [30] G.K. Sun, J.F. Young, R.J. Kirkpatrick, The role of Al in C-S-H: NMR, XRD, and compositional results for precipitated samples, *Cement and Concrete Research*, 36 (2006) 18-29.
- [31] X. Pardal, I. Pochard, A. Nonat, Experimental study of Si-Al substitution in calcium-silicate-hydrate (C-S-H) prepared under equilibrium conditions, *Cement and Concrete Research*, 39 (2009) 637-643.
- [32] P. Faucon, A. Delagrave, C. Richet, J.M. Marchand, H. Zanni, Aluminum incorporation in calcium silicate hydrates (C-S-H) depending on their Ca/Si ratio, *The Journal of Physical Chemistry B*, 103 (1999) 7796-7802.
- [33] E.M. L'Hôpital, B. Lothenbach, D.A. Kulik, K. Scrivener, Influence of calcium to silica ratio on aluminium uptake in calcium silicate hydrate, *Cement and Concrete Research*, 85 (2016) 111-121.
- [34] É.M. L'Hôpital, B. Lothenbach, G. Le Saoût, D. Kulik, K. Scrivener, Incorporation of aluminium in calcium-silicate-hydrates, *Cement and Concrete Research*, 75 (2015) 91-103.
- [35] É.M. L'Hôpital, B. Lothenbach, K. Scrivener, D.A. Kulik, Alkali uptake in calcium alumina silicate hydrate (C-A-S-H), *Cement and Concrete Research*, 85 (2016) 122-136.
- [36] B. Walkley, R. San Nicolas, M.-A. Sani, G.J. Rees, J.V. Hanna, J.S.J. van Deventer, J.L. Provis, Phase evolution of C-(A)-S-H/N-A-S-H gel blends investigated via alkali-activation of synthetic precursors, *Cement and Concrete Research*, (2016).
- [37] I. Odler, M. Rößler, Investigations on the relationship between porosity, structure and strength of hydrated Portland cement pastes. II. Effect of pore structure and of degree of hydration, *Cement and Concrete Research*, 15 (1985) 401-410.
- [38] I.G. Richardson, The calcium silicate hydrates, *Cement and Concrete Research*, 38 (2008) 137-158.

- [39] J.L. Provis, S.A. Bernal, Geopolymers and related alkali-activated materials, *Annual Review of Materials Research*, 44 (2014) 299-327.
- [40] P. Duxson, A. Fernández-Jiménez, J.L. Provis, G.C. Lukey, A. Palomo, J.S.J. van Deventer, Geopolymer technology: the current state of the art, *Journal of Materials Science*, 42 (2007) 2917-2933.
- [41] A. Palomo, S. Alonso, A. Fernández-Jiménez, Alkaline activation of fly ashes: NMR study of the reaction products, *Journal of the American Ceramic Society*, 87 (2004) 1141-1145.
- [42] I. Ismail, S. Bernal, J. Provis, S. Hamdan, J.J. Deventer, Drying-induced changes in the structure of alkali-activated pastes, *Journal of Materials Science*, 48 (2013) 3566-3577.
- [43] S. Brunauer, P.H. Emmett, E. Teller, Adsorption of gases in multimolecular layers, *Journal of the American Chemical Society*, 60 (1938) 309-319.
- [44] E.F. Osborn, R.C. Devries, K.H. Gee, H.M. Kraner, Optimum composition of blast furnace slag as deduced from liquidus data for the quaternary system CaO-MgO-Al<sub>2</sub>O<sub>3</sub>-SiO<sub>2</sub>, *T Am I Min Met Eng*, 200 (1954) 33-45.
- [45] F. Delaglio, S. Grzesiek, G. Vuister, G. Zhu, J. Pfeifer, A. Bax, NMRPipe: A multidimensional spectral processing system based on UNIX pipes, *J Biomol NMR*, 6 (1995) 277-293.
- [46] M. Fechtelkord, F. Stief, J.-C. Buhl, Sodium cation dynamics in nitrate cancrinite: A low and high temperature <sup>23</sup>Na and <sup>1</sup>H MAS NMR study and high temperature Rietveld structure refinement, *American Mineralogist*, 86 (2001) 165-175.
- [47] S.D. Wang, K.L. Scrivener, Hydration products of alkali-activated slag cement, *Cement and Concrete Research*, 25 (1995) 561-571.
- [48] P. Duxson, G.C. Lukey, F. Separovic, J.S.J. van Deventer, Effect of alkali cations on aluminum incorporation in geopolymeric gels, *Ind Eng Chem Res*, 44 (2005) 832-839.
- [49] S.A. Bernal, E.D. Rodriguez, R.M. de Gutierrez, M. Gordillo, J.L. Provis, Mechanical and thermal characterisation of geopolymers based on silicate-activated metakaolin/slag blends, *Journal of Materials Science*, 46 (2011) 5477-5486.
- [50] L. Alarcon-Ruiz, G. Platret, E. Massieu, A. Ehlacher, The use of thermal analysis in assessing the effect of temperature on a cement paste, *Cement and Concrete Research*, 35 (2005) 609-613.
- [51] B. Lothenbach, G. Le Saoût, E. Gallucci, K. Scrivener, Influence of limestone on the hydration of Portland cements, *Cement and Concrete Research*, 38 (2008) 848-860.
- [52] S.A. Bernal, R.M. de Gutierrez, J.L. Provis, V. Rose, Effect of silicate modulus and metakaolin incorporation on the carbonation of alkali silicate-activated slags, *Cement and Concrete Research*, 40 (2010) 898-907.
- [53] M.S. Morsy, Effect of temperature on hydration kinetics and stability of hydration phases of metakaolin-lime sludge-silica fume system, *Ceramics-Silikaty*, 49 (2005) 237-241.
- [54] E. Kanazaki, Thermal behavior of the hydrotalcite-like layered structure of Mg and Al-layered double hydroxides with interlayer carbonate by means of in situ powder HTXRD and DTA/TG, *Solid State Ionics*, 106 (1998) 279-284.

- [55] K. Rozov, U. Berner, C. Taviot-Gueho, F. Leroux, G. Renaudin, D. Kulik, L.W. Diamond, Synthesis and characterization of the LDH hydrotalcite–pyroaurite solid-solution series, *Cement and Concrete Research*, 40 (2010) 1248-1254.
- [56] F.J. Trojer, Crystal structure of parawollastonite, *Naturwissenschaften*, 54 (1967) 536-536.
- [57] R.J. Myers, É.M. L'Hôpital, J.L. Provis, B. Lothenbach, Effect of temperature and aluminium on calcium (alumino)silicate hydrate chemistry under equilibrium conditions, *Cement and Concrete Research*, 68 (2015) 83-93.
- [58] A.L. Gameiro, A.S. Silva, M.d.R. Veiga, A.L. Velosa, Lime-metakaolin hydration products: A microscopy analysis, *Materials and Technology*, 46 (2012).
- [59] W. Franus, R. Panek, M. Wdowin, SEM Investigation of Microstructures in Hydration Products of Portland Cement, in: E.K. Polychroniadis, Y.A. Oral, M. Ozer (Eds.) 2nd International Multidisciplinary Microscopy and Microanalysis Congress: Proceedings of InterM, October 16-19, 2014, Springer International Publishing, Cham, 2015, pp. 105-112.
- [60] R.R. Lloyd, J.L. Provis, J.S.J. van Deventer, Microscopy and microanalysis of inorganic polymer cements. 1: remnant fly ash particles, *Journal of Materials Science*, 44 (2009) 608-619.
- [61] I. Ismail, S.A. Bernal, J.L. Provis, R. San Nicolas, S. Hamdan, J.S.J. van Deventer, Modification of phase evolution in alkali-activated blast furnace slag by the incorporation of fly ash, *Cement and Concrete Composites*, 45 (2014) 125-135.
- [62] J.S.J. van Deventer, R. San Nicolas, I. Ismail, S.A. Bernal, D.G. Brice, J.L. Provis, Microstructure and durability of alkali-activated materials as key parameters for standardization, *Journal of Sustainable Cement-Based Materials*, 4 (2014) 116-128.
- [63] R.R. Lloyd, The durability of inorganic polymer cements, *Chemical and Biomolecular Engineering*, The University of Melbourne, Melbourne, Australia, 2008.
- [64] S.J. Mills, A.G. Christy, J.-M.R. Génin, T. Kameda, F. Colombo, Nomenclature of the hydrotalcite supergroup: natural layered double hydroxides, *Miner. Mag.*, 76 (2012) 1289-1336.
- [65] P. Yu, R.J. Kirkpatrick, B. Poe, P.F. McMillan, X. Cong, Structure of calcium silicate hydrate (C-S-H): Near-, mid-, and far-infrared spectroscopy, *Journal of the American Ceramic Society*, 82 (1999) 742-748.
- [66] J.A. Gadsden, *Infrared spectra of minerals and related inorganic compounds*, Butterworths, London, 1975.
- [67] P. Pena, J.M. Rivas Mercury, A.H. de Aza, X. Turrillas, I. Sobrados, J. Sanz, Solid-state  $^{27}\text{Al}$  and  $^{29}\text{Si}$  NMR characterization of hydrates formed in calcium aluminate–silica fume mixtures, *Journal of Solid State Chemistry*, 181 (2008) 1744-1752.
- [68] V. Sreeja, T.S. Smitha, D. Nand, T.G. Ajithkumar, P.A. Joy, Size Dependent Coordination Behavior and Cation Distribution in  $\text{MgAl}_2\text{O}_4$  Nanoparticles from  $^{27}\text{Al}$  Solid State NMR Studies, *The Journal of Physical Chemistry C*, 112 (2008) 14737-14744.
- [69] F. Bonk, J. Schneider, M.A. Cincotto, H.c. Panepucci, Characterization by multinuclear high-resolution NMR of hydration products in activated blast-furnace slag pastes, *Journal of the American Ceramic Society*, 86 (2003) 1712-1719.

- [70] X. Pardal, F. Brunet, T. Charpentier, I. Pochard, A. Nonat,  $^{27}\text{Al}$  and  $^{29}\text{Si}$  solid-state NMR characterization of calcium-aluminosilicate-hydrate, *Inorganic chemistry*, 51 (2012) 1827-1836.
- [71] M.D. Andersen, H.J. Jakobsen, J. Skibsted, Incorporation of aluminum in the calcium silicate hydrate (C-S-H) of hydrated Portland cements: A high-field  $^{27}\text{Al}$  and  $^{29}\text{Si}$  MAS NMR investigation, *Inorganic chemistry*, 42 (2003) 2280-2287.
- [72] P.J. Sideris, F. Blanc, Z. Gan, C.P. Grey, Identification of cation clustering in Mg-Al layered double hydroxides using multinuclear solid state nuclear magnetic resonance spectroscopy, *Chemistry of Materials*, 24 (2012) 2449-2461.
- [73] M.D. Andersen, H.J. Jakobsen, J. Skibsted, A new aluminium-hydrate species in hydrated Portland cements characterized by  $^{27}\text{Al}$  and  $^{29}\text{Si}$  MAS NMR spectroscopy, *Cement and Concrete Research*, 36 (2006) 3-17.
- [74] B. Lothenbach, A. Gruskovnjak, Hydration of alkali-activated slag: Thermodynamic modelling, *Advances in Cement Research*, 19 (2007) 81-92.
- [75] M. Moesgaard, R. Keding, J. Skibsted, Y. Yue, Evidence of intermediate-range order heterogeneity in calcium aluminosilicate glasses, *Chemistry of Materials*, 22 (2010) 4471-4483.
- [76] J.B. Murdoch, J.F. Stebbins, I.S.E. Carmichael, High-resolution  $^{29}\text{Si}$  NMR study of silicate and aluminosilicate glasses: the effect of network-modifying cations, *American Mineralogist*, 70 (1985) 370-382.
- [77] P. Florian, E. Veron, T.F.G. Green, J.R. Yates, D. Massiot, Elucidation of the Al/Si ordering in gehlenite  $\text{Ca}_2\text{Al}_2\text{SiO}_7$  by combined  $^{29}\text{Si}$  and  $^{27}\text{Al}$  NMR spectroscopy/quantum chemical calculations, *Chemistry of Materials*, 24 (2012) 4068-4079.
- [78] L.H. Merwin, A. Sebald, F. Seifert, The incommensurate-commensurate phase transition in akermanite,  $\text{Ca}_2\text{MgSi}_2\text{O}_7$ , observed by in-situ  $^{29}\text{Si}$  MAS NMR spectroscopy, *Physics and Chemistry of Minerals*, 16 (1989) 752-756.
- [79] M.R. Hansen, H.J. Jakobsen, J. Skibsted,  $^{29}\text{Si}$  chemical shift anisotropies in calcium silicates from high-field  $^{29}\text{Si}$  MAS NMR spectroscopy, *Inorganic chemistry*, 42 (2003) 2368-2377.
- [80] J. Hjorth, J. Skibsted, H.J. Jakobsen,  $^{29}\text{Si}$  MAS NMR studies of portland cement components and effects of microsilica on the hydration reaction, *Cement and Concrete Research*, 18 (1988) 789-798.
- [81] X. Cong, R. James Kirkpatrick,  $^{17}\text{O}$  and  $^{29}\text{Si}$  MAS NMR study of  $\beta$ -C2S hydration and the structure of calcium-silicate hydrates, *Cement and Concrete Research*, 23 (1993) 1065-1077.
- [82] H. Viallis, P. Faucon, J.C. Petit, A. Nonat, Interaction between salts (NaCl, CsCl) and calcium silicate hydrates (C-S-H), *The Journal of Physical Chemistry B*, 103 (1999) 5212-5219.